Development of a New Approach to Characterize Firebrand Showers During Wildland-Urban Interface (WUI) Fires: a Step Towards High-Fidelity Measurements in Three Dimensions

Nicolas Bouvet
Eric D. Link
Stephen A. Fink

NIST

National Institute of Standards and Technology
U.S. Department of Commerce

Development of a New Approach to Characterize Firebrand Showers During Wildland-Urban Interface (WUI) Fires: a Step Towards High-Fidelity Measurements in Three Dimensions

Nicolas Bouvet
Eric D. Link
Stephen A. Fink
Fire Research Division
Engineering Laboratory

May 2020

U.S. Department of Commerce
Wilbur L. Ross, Jr., Secretary

National Institute of Standards and Technology
Walter Copan, NIST Director and Undersecretary of Commerce for Standards and Technology

Abstract

A new approach to characterize airborne firebrands during Wildland-Urban Interface (WUI) fires is detailed. The approach merges the following two imaging techniques in a single field-deployable diagnostic tool: (1) 3D Particle Tracking Velocimetry (3D-PTV), for time-resolved mapping of firebrand 3D trajectories, and (2) 3D Particle Shape Reconstruction (3D-PSR), to reconstruct 3D models of individual particles following the Visual Hull principle. This tool offers for the first time the possibility to simultaneously study time-resolved firebrand fluxes and firebrand size distribution to the full extent of their three-dimensional nature. Methodologies used in the present work are presented and their technical implementation are thoroughly discussed. Validation tests to confirm proper tracking/sizing of particles are detailed. The diagnostic tool is applied to a firebrand shower artificially generated at the NIST National Fire Research Laboratory. A novel graphic representation, that incorporates both the Cumulative Particle Count (CPC, particles m^{-2}) and Particle Number Flux (PNF, particles m^{-2} s^{-1}) as relevant exposure metrics, is presented and the exposure level is compared to that of an actual outdoor fire. Size distributions obtained for airborne firebrands are compared to those achieved through ground collection and strategies to improve the particle shape reconstruction method are discussed.

Key words

Table of Contents

List of Tables

List of Figures

1. Introduction

1.1. Firebrands and the WUI fire problem

It has been recently established that fire weather season length has increased globally by almost 19 % between 1979 and 2013 [1]. Continuation of such a trend, coupled with fuel and ignition sources availability, would lead to a global wildfire potential increase with significant socio-economic and ecological impacts [1]. In the U.S., this analysis is put into perspective considering the unprecedented magnitude of wildfires affecting the western states. As an example, out of the top ten most destructive wildfires in California, seven occurred in the past five years, totaling 380 000 burned hectares, over 32 000 destroyed structures and over 120 fatalities [2]. Moreover, recent projections of wildfire activity do not seem to indicate any relief, suggesting a substantial increase of the Annual Area Burned (AAB) in southern California [3] or some of the U.S. western states [4] throughout the mid-21st century. Central to the problem are the Wildland-Urban Interface (WUI) and intermix areas where human lives and regional economies have been regularly at stake in the recent years. The newly evaluated economic burden (cost + loss) of wildfires in the U.S. indicates that the issue is rather significant, the lower estimate being 71.1 billion USD/year [5]. There is currently a pressing need to intensify research in various areas (e.g., wildland/WUI fire science, building materials and construction, population alerting and evacuation, etc.), in order to minimize wildfire impacts by improving community resilience in populated zones at risk.

A challenging aspect of wildland/WUI fires lays in the fact that large amounts of firebrands (often referred to as "embers") are usually produced from the burning of vegetative and structural fuels. These firebrands often become airborne and can be transported over long distances away from their origin. If they carry enough energy, they may ignite recipient fuels and, in turn, initiate new fire fronts, rendering suppression activities extremely difficult. It is not uncommon to witness "rains" or "showers" of firebrands impacting WUI areas, a recent example being the Coffey Park neighborhood in Santa Rosa, CA, during the Tubbs Fire in 2017 [6]. It has also been confirmed through post-fire investigations that firebrand assaults are responsible for a large number of structure losses in the WUI [7]. Characterizing the exposure from firebrands impacting the WUI has therefore become a priority; quantities such as particle number/mass fluxes, particle size distribution, and particle surface temperature/energy content are still largely unknown yet necessary to provide a thorough understanding of the WUI fire hazard and facilitate its evaluation [8]. One of the outcomes of such an approach would be, for instance, to enable guidance to WUI-related building codes and standards on choosing cost-effective mitigation strategies for ignition vulnerabilities that are commensurate with the actual firebrand exposure threat.

Over the years, there have been quite a few efforts to characterize firebrands generated by structural or vegetative fuels, in both lab-scale and outdoor fire configurations. Studies have essentially focused on core characteristics of firebrand flows, including "macro" characteristics related to the number and mass of particles generated, as well as "micro" characteristics, such as individual particle size and shape. Thermal characteristics of burning firebrands have also been the subject of recent laboratory investigations (see, for instance, Refs. [9-11] for firebrand heat generation and Refs. [12, 13] for firebrand surface temperatures) but are out of the scope of the present work and will not be considered here. Firebrands produced during the burning of structural materials have been investigated for experimental configurations ranging from simple building components, i.e., wall assemblies [14-16] and roofing elements [17, 18], to

1

full scale structures, both indoor [19, 20] and outdoor [21-23]. Firebrands generated by vegetative fuels were also studied for various configurations, including the burning of single trees in laboratory conditions [24-26], as well as prescribed [27-30] and actual fires [31, 32]. In most cases [14-20, 23-25, 27-29], firebrands are captured in water pans located at ground level, dried, and further processed (manually and/or using computerized procedures) to yield the desired information. Alternatively, burn patterns in well-chosen substrates have also been analyzed [21, 22, 31, 32]. Besides being extremely time-consuming and possibly prone to random bias (e.g., breakage of firebrands at landing), these approaches present significant limitations when investigating firebrand showers characteristics at both macroscopic (bulk flow) and microscopic (individual particle) scales. These limitations are highlighted below.

(1) Considering bulk flow characteristics (e.g., particle number/mass fluxes):
- The results obtained are intrinsically time-averaged, hence information regarding instantaneous intensity of the firebrand showers is not available. To date, only the investigations by Filkov et al. [28, 30] and Tohidi et al. [26] have shown some temporal resolution ability using 2D imaging devices, but their analyses are somewhat hindered by the lack of volumetric resolution, which renders measurements of instantaneous particle fluxes extremely challenging (only time-averaged particle number fluxes are discussed in Ref. [30], and Ref. [26] only provides an estimated mass flux of firebrands generated, lacking spatial distribution information).
- The results reported only pertain to firebrand exposures that are partially characterized. For instance, when available, firebrand fluxes are solely understood based on data collection/processing performed in 2D planes oriented parallel to the ground. Hence, the simultaneous consideration of horizontal transport is overlooked although likely to be important in many practical situations (e.g., exposure severity assessment in the vicinity of structures with exposed vents, rate of firebrand deposition vs downstream transport ahead of a fire line, etc.).

(2) Considering individual particle characteristics (e.g., firebrand size/shape):
- While mass determination of individual firebrands is rather straightforward in the case of collected samples, firebrand sizing is significantly more challenging due to the three-dimensional nature of a particle. With a few exceptions (see Refs. [24, 25, 27]), a firebrand projected area, also referred to as cross section area, is routinely taken as the important metric, which considerably simplifies sizing operations by allowing 2D image processing tools to be used. Such an approach has also been considered for airborne firebrands visualized by 2D imaging systems [26, 30], although results might be difficult to interpret given the possibility of tumbling motions. Firebrand dimensions (e.g., height, width and depth of a particle "bounding box"), volumes and shapes have been mostly undetermined or neglected. These morphological attributes are expected to be important to assess the likelihood of phenomena related to particle deposition, including the formation of aggregates and trapping in complex geometries (screen mesh, crevices, etc.).

The limitations highlighted above clearly stress the need for new ways to characterize firebrand showers in the context of their three-dimensional nature, both at the macroscopic and microscopic levels. Therefore, the present work is devoted to the development and validation of a diagnostic tool designed to overcome these limitations by allowing full spatio-temporal resolution of airborne firebrand flows. To do so, this new tool merges two optical techniques, 3D Particle Tracking Velocimetry (3D-PTV) and 3D Particle Shape Reconstruction (3D-PSR)

2

in a single field-deployable device, referred to as "emberometer". More details about these techniques are given in the two following sub-sections.

1.2. 3D Particle Tracking Velocimetry (3D-PTV)

3D-PTV is a flow measurement technique geared towards the determination of velocity fields within a three-dimensional observation volume based on the time-resolved motion of particle tracers. It has been developed and refined over the past three decades and has been widely used to investigate small scale systems in laboratory configurations, often in the context of turbulent flow research (e.g., [33-35]). While traditionally applied to problems where the carrier flow dynamic is of interest (and therefore velocity fidelity of flow tracers is a concern), the technique can be equally applied to track discrete entities irrespective of the motion of the surrounding medium. As a Lagrangian approach, 3D-PTV is particularly well suited to the firebrand shower problem since particles are individually identified and their respective motion is followed over time, permitting detailed evaluation of the particle-laden flow characteristics, such as particle number fluxes, not easily obtained through Eulerian techniques (e.g., Particle Image Velocimetry - PIV). To date, only very few experimental investigations have performed 3D-PTV measurements at length scales relevant to the firebrand shower problem. Observation volumes several orders of magnitude larger than the usual cubic centimeter scale are required, which often prevents using off-the-shelf equipment, especially when outdoor use is intended. A brief overview of medium to large scale 3D-PTV investigations sharing some similarities with the present work is provided in what follows. Some of the technical details are summarized in Table 1 (provided next page). Properties of the system developed in this work are given in the last row for ease of comparison (the system itself is further described in Sec. 2.2).

Murai et al. [36] investigated the motion of luminous particles in a firework using a stereoscopic camera arrangement in outdoor settings. Particle velocities up to 70 m s^{-1} were measured and the diameter of the developed firework was found to exceed 200 m in both horizontal and vertical directions. In this work, stereo-pair matching was identified as one of the main technical challenge, essentially arising from the low voxel resolution (0.21 m^3/voxel) relative to the actual particle sizes.

Biwole et al. [37] detailed a newly developed 3D particle tracking algorithm. The algorithm incorporated an enhanced detection procedure for neutrally buoyant particles (helium-filled soap bubbles) as well as various refinements of some of the 3D-PTV processing steps. The algorithm was applied to a set of indoor airflow experiments including two rooms with light-gray (3.1 m × 3.1 m × 2.5 m) and black (5.5 m × 3.7 m × 2.4 m) walls respectively, a subpart of the room with black walls where a heat source was placed and an experimental aircraft cabin (4 m × 3 m × 2 m). The experimental setups typically included a set of three cameras, various illumination devices and an adequately positioned He-filled bubble supply. Different tracer densities were achieved in each case, with a particle spacing index (ratio of the mean particle spacing to the mean particle displacement between two consecutive frames) ranging from 8.1 (low seeding density) down to 2.1 (high seeding density). The algorithm performance was assessed using previously formulated tracking efficiency criteria [38, 39]. Velocity measurements reported in this work did not exceed 1 m s^{-1}.

3

Table 1 Medium to large scale experimental investigations using 3D Particle Tracking Velocimetry (# Cam.: number of cameras, CG: consumer-grade, CS: scientific-grade, px: pixel, FOV: Field of view, fps: frame per second, ×: not specified. The spacing index is defined as the ratio of the mean particle spacing to the mean particle displacement between two consecutive frames).

Author Year [Ref.]	3D-PTV System			Setup Details				Application
	# Cam. / Grade (Image size)	Illumination (#)	Tracers/ Particles	Control Volume	fps	Velocity range (m s^{-1})	Spacing index	
Murai et al. 2008 [36]	2 - CG (640×480) px	none	Fireworks	Unknown, FOV ≈ (300×200) m^2	30	High speed up to ≈ 70	-	Tracking of luminous particles in fireworks - *Outdoor*
Biwole et al. 2009 [37]	3 - SG (1024×1024) px	1000W fluorescent lamps (×6)	He-filled soap bubbles	Unknown, (3.1×3.1×2.5) m^3 room	100	Low speed ≈ 0.2-0.65	3.9-8.1	Indoor airflow studies (rooms and aircraft cabin) - *Indoor*
	3 - × (×)	500W spotlights (×6)	He-filled soap bubbles	10.8 m^3	30	Low speed ≈ 0.015-0.52	2.2-3.3	
	3 - × (×)	Spotlights (×2)	He-filled bubbles	≈ 2 m^3	×	Low speed up to ≈ 0.85	3.3-4.8	
	3 - × (×)	120W light bulbs (×8) + 500W spots (×2)	He-filled bubbles	Unknown, (4×3×2) m^3 cabin	×	×	2.1-2.3	
Lobutova et al. 2010 [40]	4 - CG (8) Mpx	High power flash lamps (×2)	He-filled latex balloons (∅: 150 mm)	≈ 100 m^3	1	Low speed < 0.6	×	Large-scale circulations in room air flows (Rayleigh Bénard cell) - *Indoor*
Rosi et al. 2014 [41]	4 - CG (1280×720) px	none	Fog-filled soap bubbles (∅: 25 mm)	16 m^3	60	< 4.5	7.5	Wind speed measurements in the lower log region of the atmospheric surface layer – *Outdoor*. Also see Ref. [42]
This study	4 - CG (1920×1080) px	none	Glowing firebrands	≈ 2 m^3	120	0.2-4.5 (¼ max fps) (≈ 18, max fps)	-	Firebrand motion *Indoor/Outdoor*

4

Lobutova et al. [40] studied large-scale air flow patterns in a Rayleigh-Bénard experimental facility (≈ 144 m^3) using the 3D-PTV approach. Their system was composed of four consumer-grade cameras, two high-power flash lamps for illumination, and helium-filled latex balloons ($\varnothing = 150$ mm) as tracers. The system accuracy was checked by monitoring the known trajectory of a glass sphere attached to a stepping motor; error margins were found not to exceed 2.4 mm in the horizontal plane and 0.8 mm in the vertical direction. Trajectories of large-scale air circulations were measured in the bulk region of the convection cell at an acquisition rate of 1 Hz over periods ranging from 1 min to 20 min. Different flow patterns were identified, and their temporal and spatial properties were briefly discussed, including some aspects related to flow turbulence. Velocity components of large scale circulations reported in Ref. [40] did not exceed 0.6 m s^{-1}.

Rosi et al. [41] studied wind velocity profiles in the lower log region of the atmospheric surface layer using an adaptable 3D-PTV system designed for outdoor use. The system was composed of four consumer-grade cameras arranged to monitor a 16 m^3 observation volume, with a center located 3 m above ground. Fog-filled bubbles ($\varnothing = 25$ mm), released 30 m ahead of the zone of interest, were used as tracers (no illumination required). The system calibration procedure led to a spatial uncertainty of 10 mm. Validation was provided by comparing measurements (mean velocities, Reynolds stresses) to those obtained by a wind measurement station located nearby. Probability distribution functions of the velocity fluctuations, Lagrangian accelerations and vorticities were presented and discussed. The highest mean velocity measured by the 3D-PTV system was close to 4 m s^{-1}.

1.3. 3D Particle Shape Reconstruction (3D-PSR) based on the Visual Hull concept.

The use of multi-view systems to track firebrands in 3D also renders possible the reconstruction of individual particle shapes. Such 3D models can provide valuable insights regarding particle characteristic sizes, volume, and shape that are not otherwise available using single-view imaging techniques. Typically, several 2D images of a particle are recorded simultaneously from different viewpoints. The particle images, often referred to as particle *silhouettes*, can be projected towards the measurement domain provided that the optical arrangement is known. The intersection of all projection cones defines an envelope that corresponds to the 3D shape of the particle (surface-based approach). Alternatively, the measurement domain can be subdivided into elemental volumetric cells, and the 3D shape recovered by only retaining cells that fulfill a specified criterion, e.g. cells whose projections fall back into all silhouette contours (volume-based approach). In both cases, the reconstructed volume, referred to as *visual hull*, corresponds to the largest volumetric domain that would give identical silhouettes as the particle when observed from each of the different 2D views.

A simplified illustration of the surface-based approach is given in Fig. 1 for a setup involving two imaging devices. It is clear from Fig. 1 that the higher the number of imaging devices, the closer the visual hull gets to the actual particle shape. The main limitation, however, is that regions with surface concavities cannot be reproduced since they do not alter the particle silhouette shapes.

5
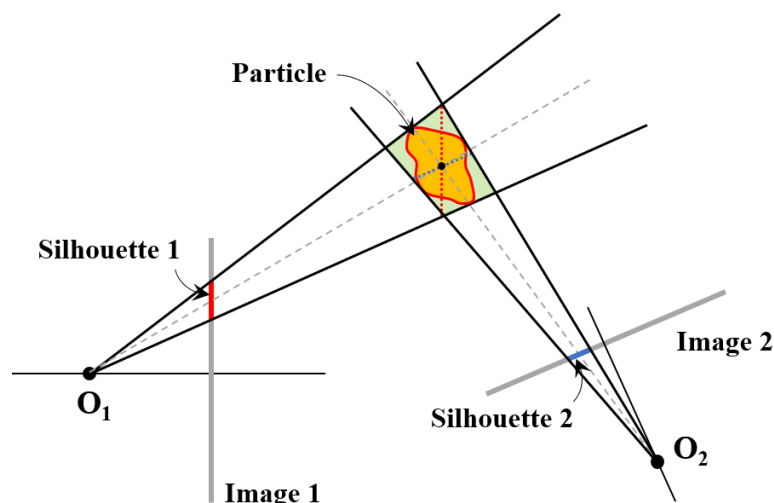
Fig. 1. Simplified 2D sketch illustrating the Visual Hull concept for 3D particle shape reconstruction (O_i : imaging device perspective center).

The Visual Hull concept, first formulated by Laurentini [43], is widely used in computer vision whenever 3D shape reconstruction is needed based on multi-view silhouette observations. The fields of application are numerous including medical imagery, human motion tracking, particle morphology analysis in geosciences, etc. Therefore, providing a thorough review of this topic would go beyond the scope of this work. In the present case, the reader is referred to the work of Forbes [44] that provides a concise description of the concept as applied to the 3D reconstruction of small stones and discusses some of the issues related to its practical implementation. Studies that have implemented the Visual Hull approach in order to extract particle characteristics (e.g., size, volume or shape) are scarce in the literature, especially those providing a detailed assessment of the technique performance. A brief summary of the relevant works is provided in what follows. Some technical details are also provided in Table 2 (see next page).

Forbes [44] discussed a multi-camera setup to investigate the shape and size of batches of small stones ($\approx$ 5 mm) using the Visual Hull concept. The setup was composed of six cameras judiciously positioned onto six of the twelve faces of a fictitious dodecahedron. The working distance was about 500 mm for all cameras. The methodology developed in Ref. [44] was applied to synthetic garnet data with known properties for a configuration identical to the actual six-camera setup described above. For sufficiently resolved silhouettes, the mean percentage error between the actual (true) and estimated (visual hull) volumes was found to be close to 8 %. Additional virtual camera arrangements were also considered, and these led to errors on the order of 41 %, 20 %, 14 %, and 5 % for a two-, three-, four- and ten-camera setup, respectively. These percentages indicated a systematic overestimation of the true stone volumes, which was deemed consistent given the principles of the Visual Hull method. Caliper diameter estimations were also performed on the synthetic dataset for the six-view system, and mean percentage errors on the order of 4 %, 0.8 %, and 0.5 % were obtained for the shortest, intermediate and longest diameters, respectively. Other hull-based reconstruction approaches, especially the Viewing Edge Midpoints Hull (VEMH), were also extensively discussed by the author.

Table 2 Summary of experimental investigations using the Visual Hull approach for particle size/shape characterization
(# Cam.: number of cameras, px: pixel, WD: working distance, ×: not specified).

Author Year [Ref.]	Object		Optical Arrangement			Note on Particle Reconstruction Accuracy
	Type	Size Range	# Cam.	(Image size)	WD	
Forbes 2007 [44]	Stones	≈ 5 mm	6	×	≈ 0.5 m	- Mean percentage error close to 8 % for volume reconstructions (ranging from 41 % to 5 % for a two- to ten-camera setup - virtual camera arrangements). - Mean percentage errors on the order of 4 %, 0.8 %, and 0.5 % for the shortest, intermediate and longest particle diameters, respectively (performed on a synthetic dataset).
Turchiuli and Castillo-Castadena 2009 [45]	Dehydrated milk agglomerates	1 mm – 2 mm	1 (object placed on rotating platform)	(102×63) px	Few cm	- Verification test performed on a large object (≈ 25 mm) showed measured volume to be 4.4 % larger than true value. - Accuracy of the technique mentioned to be on the order of 90 %.
Adhikari and Longmire 2012 [46]	Solid objects with known shape	8 mm (characteristic length)	4	(1280×800) px	≈ 0.6 m	- Volume ratios between estimated and actual objects ranging from 1.3 (sphere and cylinder) up to 3.9 (tetrahedron).
Rajagopalan et al. 2017 [47]	Crystals	< 200 um	2	×	×	- Particle size validation test performed but characteristics inferred from individual particle silhouettes only rather than reconstructed hulls.
Kleinkort et al. 2017 [48]	Snowflakes	Few mm	5	3× (5) Mpx 2× (1.2) Mpx	0.1 m 0.16 m	- Reconstructed volume of synthetic sphere (diam.: 3 mm) found to be 5.3 % larger than true value. - Volume overestimations found to range between 1.65 % to 46.33 % for objects with various shapes (sphere, cube, cylinder, etc.).
This study	Firebrands	Few mm to few cm	4	(1920×1080) px	≈ 1.2 m - 2.8 m	See Sections 3.2, 4.2.3 and 5.

Turchiuli and Castillo-Castadena [45] used the Visual Hull concept to measure envelope volumes of dehydrated milk agglomerates in the context of powder porosity studies. Agglomerates ($\approx$ 1 mm to 2 mm) were placed on a rotating platform in proximity (few centimeters) of a calibrated camera. Particle silhouette images (likely 18 of them), taken at an angular increment of 10°, were used to reconstruct the 3D shape of the agglomerates by identifying voxels belonging to the intersection of all solid projection cones. A verification test performed on a large object ($\approx$ 25 mm) showed that the estimated volume was almost 4.4 % larger than the true value. However, the accuracy of the technique is argued to be on the order of 90 % given the image acquisition settings chosen. It is unclear from the author's statement if this percentage corresponds to a 10 % over- or under- estimation of the volumes. Under-resolved silhouette images have been shown to lead to volume underestimations [44]; this could be the case here given the rather low pixel resolution ((102×63) px).

Adhikari and Longmire [46] used the Visual Hull technique to reconstruct arbitrary moving objects falling in a water tank and to study flow motion around them using tomographic PIV. Their setup consisted of a set of four high speed cameras ((1280×800) px) operating at 1 kHz. The cameras, located on the same side of the illumination plane, were equipped with 105 mm focal length lenses and were set about 600 mm away from the measurement volume. Examples of 3D reconstructions were given for objects encompassing various shapes, sharing a common characteristic length of 8 mm; volume ratios between the estimated and actual objects ranged from 1.3 for a sphere and a cylinder, up to 3.9 for a tetrahedron. The presence of additional volumes in the front and the back of the reconstructed shapes was discussed, including factors encompassing particle size, orientation and convexity. Ways to improve the technique by modifying camera arrangements (e.g. change of orientation, camera additions) were also covered.

Rajagopalan et al. [47] described the development and validation of an experimental device designed to characterize particle shape and sizes during crystallization processes occurring in a reactor. The device consisted of two monochrome cameras equipped with telecentric optics (FOV $\approx$ 2.41 mm $\times$ 2.02 mm), arranged orthogonally around the channel of a flow sampling loop. Shapes of crystals in suspension were reconstructed in 3D using the Visual Hull technique (voxel-based approach) applied to the crystal silhouette pairs. A supervised shape classification strategy, involving a set of 2D/3D particle shape descriptors and proper shape classifiers, was proposed. Particle size validation was performed using sets of spherical latex beads of known sizes. However, the particle size characteristics (diameter, volume) were inferred from the particle silhouette images rather than the reconstructed hulls (see supplemental material in Ref. [47]). The authors acknowledged the use of only two cameras as one of the key limitations for accurate Visual Hull reconstruction, although they question the need for adding extra cameras given the resulting higher costs and system complexity and a possibly marginal gain of knowledge.

Kleinkort et al. [48] reported on the development and validation of an experimental approach to characterize the shape of snowflakes in order to support accurate computation of polarimetric radar measurables for winter precipitations. A new snowflake imaging device, based on the work of Garrett et al. [49], was presented. The device was made of five cameras (3× 5-Mpx, 2× 1.2-Mpx) equipped with 12.5 mm focal length lenses (working distance of 10 cm and 16 cm, respectively) and arranged to closely monitor the center of a channel along which free-falling hydrometeors could be imaged. Three dimensional shapes of snowflakes

8

were reconstructed following the Visual Hull concept (voxel-based approach) using the five-camera views. The 3D reconstruction accuracy was tested by processing a set of synthetic images representing a 3 mm diameter sphere. The reconstructed volume was found to be 5.3 % larger than the actual one, which was almost 22 % less than the estimate obtained using the three-camera configuration of Ref. [49]. The five-camera setup was tested using series of 3D printed particles of known sizes and shapes (sphere, cube, cylinder, flat hexagon and simple flakes). A systematic overestimation of the reconstructed volumes was reported, with errors ranging from 1.65 % to 46.33 % for all cases. The technique was applied to a series of real snowflakes to extract properties such as volume, surface area and aspect ratio. In this case, however, the level of accuracy achieved is unclear given the fractal nature of the flakes (is the resolution enough given the smallest length scale involved?), complexity of geometries (presence of inner voids, concavities) as well as optical arrangement issues (out of focus images).

1.4. Paper layout

The remaining part of the paper is organized as follows: Sec. 2 provides a detailed overview of the 3D-PTV/PSR system that was developed in the present work. It includes a short preamble on key principles of close-range photogrammetry, followed by hardware presentation and details about methodology implementation. Examples of experimental validations performed for both particle tracking and sizing steps are given in Sec. 3. The system is applied to an artificially-generated firebrand shower in Sec. 4. Particle tracking and sizing results are discussed and a new visualization tool for firebrand flux analysis is proposed. Final remarks are provided in Sec. 5, followed by the conclusion in Sec. 6.

Unless mentioned otherwise, all uncertainties are reported as expanded uncertainties, $X \pm k\,u_c$, from a combined standard uncertainty (estimated standard deviation) u_c, and a coverage factor $k = 2$ (95 % confidence level, assuming normal distribution of the data). Additional details are provided in the Appendix A.

2. 3D-PTV/PSR system

2.1. 3D imaging using close-range photogrammetry

This section intends to provide the reader with key principles of 3D imaging along with useful mathematical expressions used to derive some of the results presented in later sections. For in-depth coverage of the topic, the reader is referred to reference textbooks, e.g. Ref. [50]. In brief, photogrammetry is an imaging technique that allows for the localization of an object in 3D, using at least two images of the object taken from two different angles/viewpoints. Each system recording an image can be thought of as a pinhole camera (see Fig. 2): rays of light emanating from the object enter the imaging device through a small opening O, known as the *perspective center*. The image of the object is formed in the *image plane* (that, in practice, coincides with the sensor of the imaging device). The *image plane* is located at a fixed distance c from the *perspective center*, this distance being commonly referred to as the *principal distance*. The *principal point* G' is defined as the intersection of the system *principal axis* with the *image plane*.
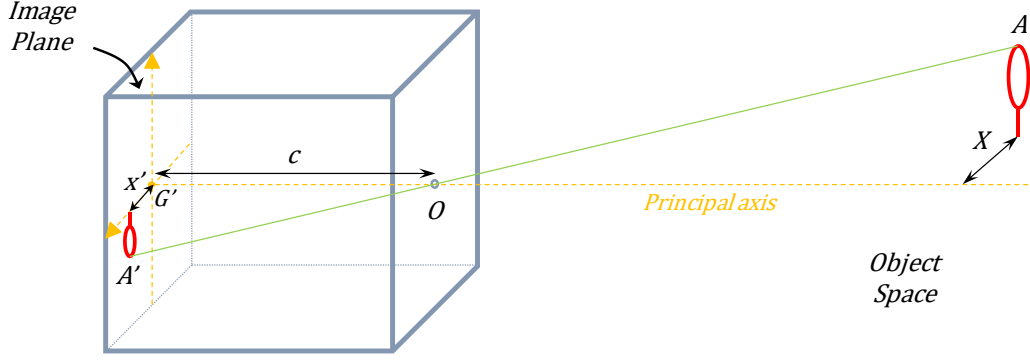
Fig. 2. Schematic representation of a pinhole camera, base model for the cameras of the 3D-PTV system (O: perspective center, G': principal point, c: principal distance).

To successfully apply photogrammetry, imaging devices need to be calibrated. The calibration typically accounts for 2 sets of orientation parameters:

(1) internal (or intrinsic) parameters (Fig. 3a). These are used to establish the correspondence between the coordinates of an image point A' located in the 2D image space (colored image planes in Fig. 3a) and its coordinates in a 3D image space defined by the reference frame $x^*y^*z^*$, whose origin coincides with the perspective center O of the imaging device. In practice, the model is not as ideal as the one depicted in Fig. 2, since the principal point G' might not coincide with the center of the image. Also, optical distortions (e.g. barrel, pincushion, etc.) might affect the location of an image point in the 2D image space (recorded by the imaging sensor) so that it differs from its actual location as predicted by the central projection model (see A'' vs. A' in Fig. 3a). Considering both possible deviations, the coordinates (x', y', z') of an image point A' in the 3D image space can be found as follows:

$$\begin{bmatrix} x' \\ y' \\ z' \end{bmatrix} = \begin{bmatrix} x'' - x_{G'} - \delta x' \\ y'' - y_{G'} - \delta y' \\ -c \end{bmatrix} \tag{1}$$

with x'' and y'', the coordinates of the image point A'' in the 2D image space (as recorded by the imaging sensor), $x_{G'}$ and $y_{G'}$, the coordinates of the principle point G' in the 2D image space, and $\delta x'$ and $\delta y'$, errors in the image point positioning arising from optical distortions. Note that Eq. (1) is written for the image positive (orange frame in Fig. 3a) which is often taken as the image reference plane in photogrammetry applications.

(2) external (or extrinsic) parameters (Fig. 3b). These parameters describe the location and orientation of the reference frame $x^*y^*z^*$ with respect to a main reference frame XYZ attached to the object space. These parameters can be used to establish correspondence between a point (X, Y, Z) in the 3D object space and its image (x', y', z') in the 3D image space:

$$\begin{bmatrix} X \\ Y \\ Z \end{bmatrix} = \begin{bmatrix} X_0 \\ Y_0 \\ Z_0 \end{bmatrix} + m\,\boldsymbol{R} \begin{bmatrix} x' \\ y' \\ z' \end{bmatrix} \tag{2}$$

10

with X_0, Y_0 and Z_0, the coordinates of the perspective center in the object space, m, a scaling factor depending on the location of the object point, and $\boldsymbol{R}$, the rotation matrix, expressed as:

$$\boldsymbol{R} = \begin{bmatrix} r_{11} & r_{12} & r_{13} \\ r_{21} & r_{22} & r_{23} \\ r_{31} & r_{32} & r_{33} \end{bmatrix}$$

$$= \begin{bmatrix} \cos\varphi\cos\kappa & -\cos\varphi\sin\kappa & \sin\varphi \\ \cos\omega\sin\kappa + \sin\omega\sin\varphi\cos\kappa & \cos\omega\cos\kappa - \sin\omega\sin\varphi\sin\kappa & -\sin\omega\cos\varphi \\ \sin\omega\sin\kappa - \cos\omega\sin\varphi\cos\kappa & \sin\omega\cos\kappa + \cos\omega\sin\varphi\sin\kappa & \cos\omega\cos\varphi \end{bmatrix}$$

(3)

with ω, φ and κ rotation angles around the X, Y and Z axes, respectively. Introducing Eq. (1) in Eq. (2) and solving for x'' and y'' leads to the *collinearity equations*:

$$x'' = x_{G'} - c\,\frac{r_{11}(X - X_0) + r_{21}(Y - Y_0) + r_{31}(Z - Z_0)}{r_{13}(X - X_0) + r_{23}(Y - Y_0) + r_{33}(Z - Z_0)} + \delta x' \tag{4}$$

$$y'' = y_{G'} - c\,\frac{r_{12}(X - X_0) + r_{22}(Y - Y_0) + r_{32}(Z - Z_0)}{r_{13}(X - X_0) + r_{23}(Y - Y_0) + r_{33}(Z - Z_0)} + \delta y' \tag{5}$$

Note that all internal (c, $x_{G'}$, $y_{G'}$, $\delta x'$, $\delta y'$) and external (X_0, Y_0, Z_0, ω, φ, κ) orientation parameters are device-dependent, and therefore, each imaging device should be calibrated. More details about the calibration procedure are given in Sec. 2.3.2.
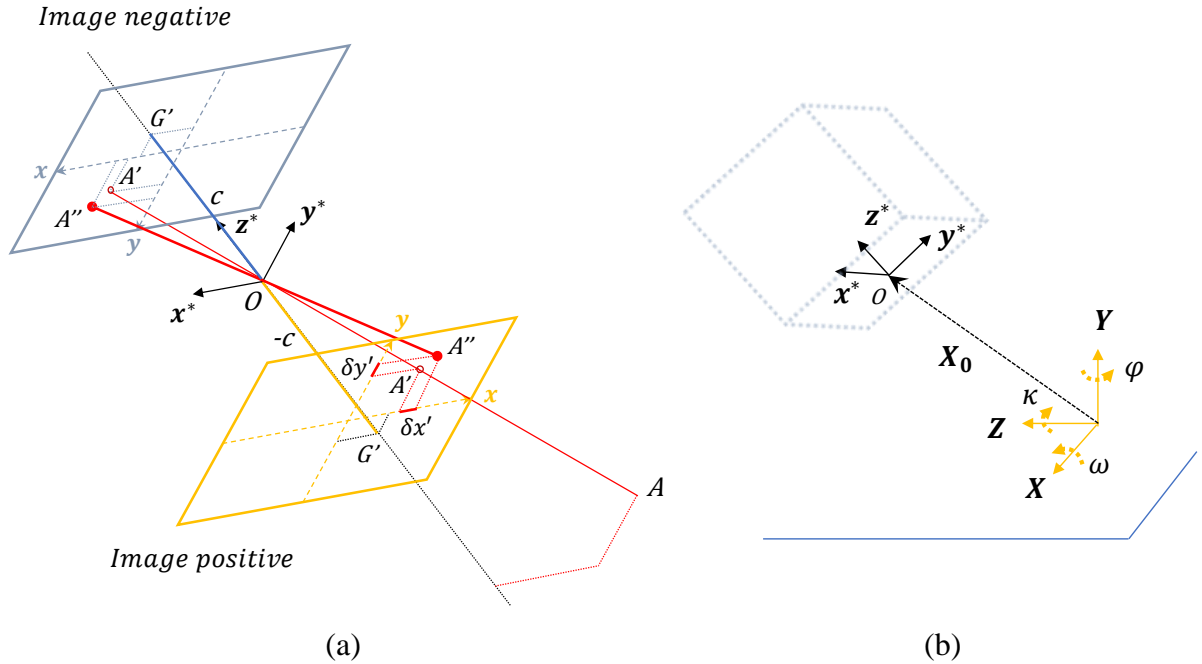
Fig. 3. 3D-PTV camera orientation parameters; (a) internal parameters; (b) external parameters.

11

It is clear looking at Eqs. (4) and (5) that the 3D coordinates (X, Y, Z) of an object point cannot be solely found using the 2D image point coordinates (x'', y'') and that at least two images taken with calibrated devices (with different orientations) are needed. In the latter case, correspondence between image points across the different views can be established using *epipolar geometry* [51, 52], and the object point coordinates can be computed. Taking the example of the two-camera setup shown in Fig. 4, *epipolar geometry* implies that both perspective centers O_1 and O_2 and images points A_1 and A_2 lay in a single plane. This plane, referred to as the *epipolar plane*, intersects the image planes along the *epipolar lines* d_1 and d_2 (red lines in Fig. 4). Given the coplanarity condition, the search in image 2 for the image point corresponding to A_1 is simplified, since it only needs to be performed along the line d_2. In practice, the search is usually limited to a narrow band-shaped area (in orange in Fig. 4) if the depth L of the object space is known (hence limiting the longitudinal search in the image space to the distance l) and a transverse search tolerance e allowed. By intersecting the search areas across additional views (3rd, 4th, etc. imaging devices), the correspondence between image points can be unambiguously established and coordinates of the object point A calculated, for instance performing least square adjustment using the collinearity equations.
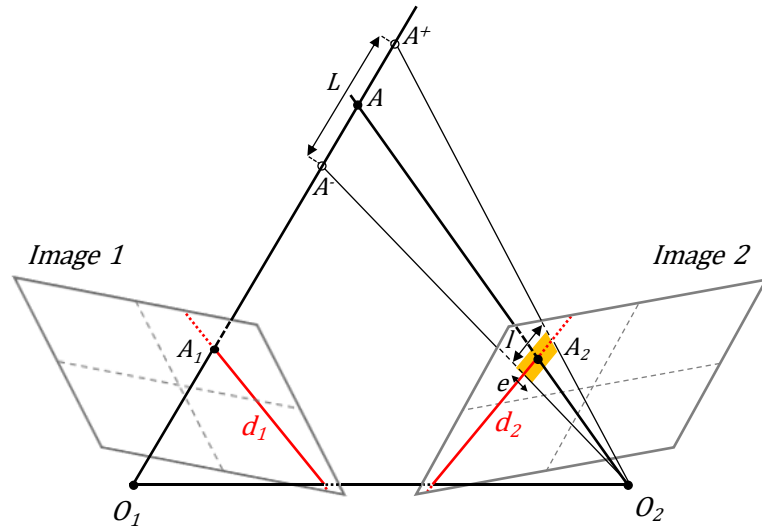
Fig. 4. Illustration of the epipolar line geometry in the case of two imaging devices (adapted from Ref. [52]).

2.2. System overview[1]

2.2.1. Experimental layout

The 3D representation of the 3D-PTV/PSR system is shown in Fig. 5a. The system is composed of four compact cameras (*Sony DSC-RX10 M3*, ≈ 20.1 Megapixels) with large diameter built-in lenses. The cameras are located at both ends of two horizontal rails (length:

---

[1] Certain commercial equipment, instruments, or materials are identified in this paper in order to specify the experimental procedure adequately. Such identification is not intended to imply recommendation or endorsement by the National Institute of Standards and Technology, nor is it intended to imply that the materials or equipment identified are necessarily the best available for the purpose.

2.03 m), whose upper faces are adjusted at a 0.356 m and 1.880 m height, respectively. Both rails are supported by a mobile stand, allowing the entire system to be moved without performing additional calibrations. In the current settings (calibration/validation), the stand is anchored to an optical table (≈ 1.22 m $\times$ 1.22 m) located 0.559 m away from the camera plane. The table top, raised by about 0.235 m from the ground, provides a convenient fixed reference in the object space. The origin of the global object coordinate system is set at table height, 0.711 m and 0.610 m from its front and side edges, respectively. Camera orientations (tilt about horizontal axis, azimuth) are manually adjusted using tripod heads so that image centers closely coincide with a known target point T in the object space (coordinates (0 m, 1.041 m, 0 m)), on which focus is performed. Each camera is equipped with a collimated laser diode module (*Thorlabs, CPS series*) and all laser beams are set to intersect at point T. This arrangement simplifies subsequent setups by providing a visual marker in space (invariant position) that can be used to complete camera focusing steps. It is also used at the beginning of each experiment to detect any unwanted change of camera orientation. Cameras are operated at minimum focal length ($f = 8.8$ mm) and largest aperture ($f/2.4$). As such, the system control volume is defined as the intersection of the camera field of views, corrected for small volumes not accounted for during the spatial calibration process. The control volume is shown in Fig. 5b and is estimated to be ≈ 1.91 m^3.

(a)   (b)
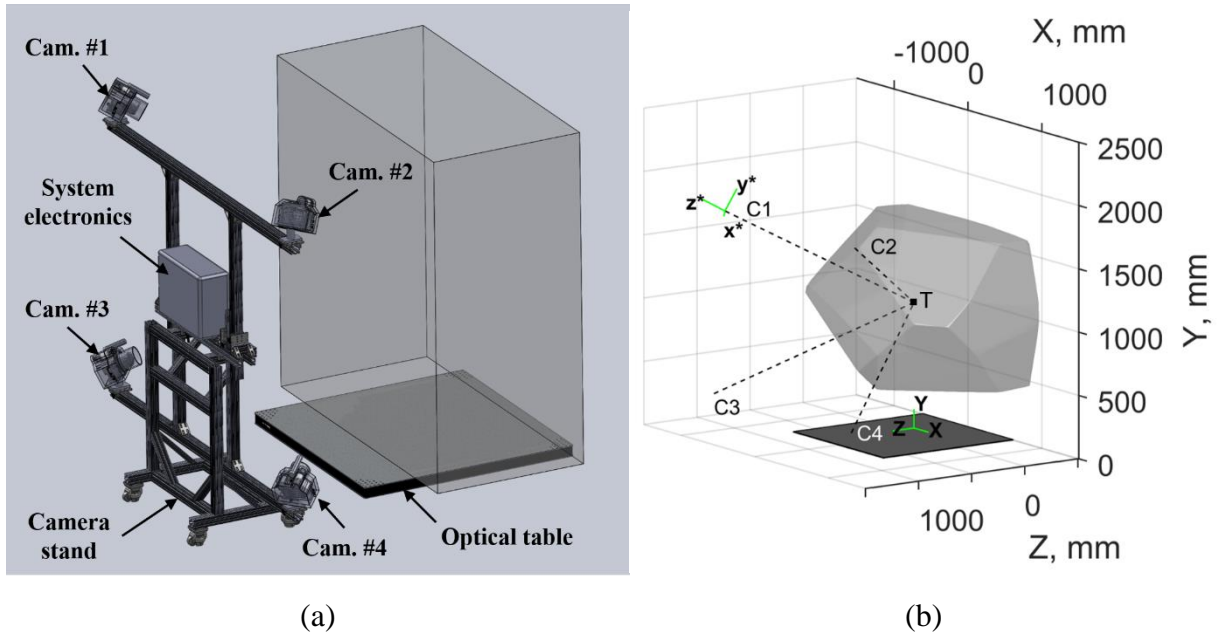
Fig. 5. 3D-PTV/PSR system experimental layout; (a) 3D representation of the apparatus (the volume above the optical table shows the actual footprint of the spatial calibration target shown in Fig. 7a); (b) Simplified schematic showing the optical layout and actual control volume.

2.2.2. System control / data acquisition

Near-field triggering of the camera system is performed using a remote commander and a set of IR wireless receivers (*Sony RMT-VP1K*). Videos are captured in High Definition ((1920×1080) px) at a nominal rate of 120 fps. Video streams are synchronized post-acquisition based on the disappearance of a small laser dot manually operated by the user and visible from all cameras. Proper synchronization was verified by imaging a millisecond

13

precision digital counter. The synchronization error was found to be within the time lapse between two consecutive frames, up to the highest available frame rate (960 fps). Alternatively, long range operation of the system is achieved using a custom-developed control hub (*CAMremote-4CAM*, *VP-Systems*) that allows for remotely adjusting camera settings as well as triggering cameras/sync laser via RF control (433.92 MHz). The control hub is part of a self-contained, ruggedized package (shown in Fig. 5a) that also includes wireless video monitoring and power management systems. Additional details are given elsewhere [53].

2.2.3. Processing
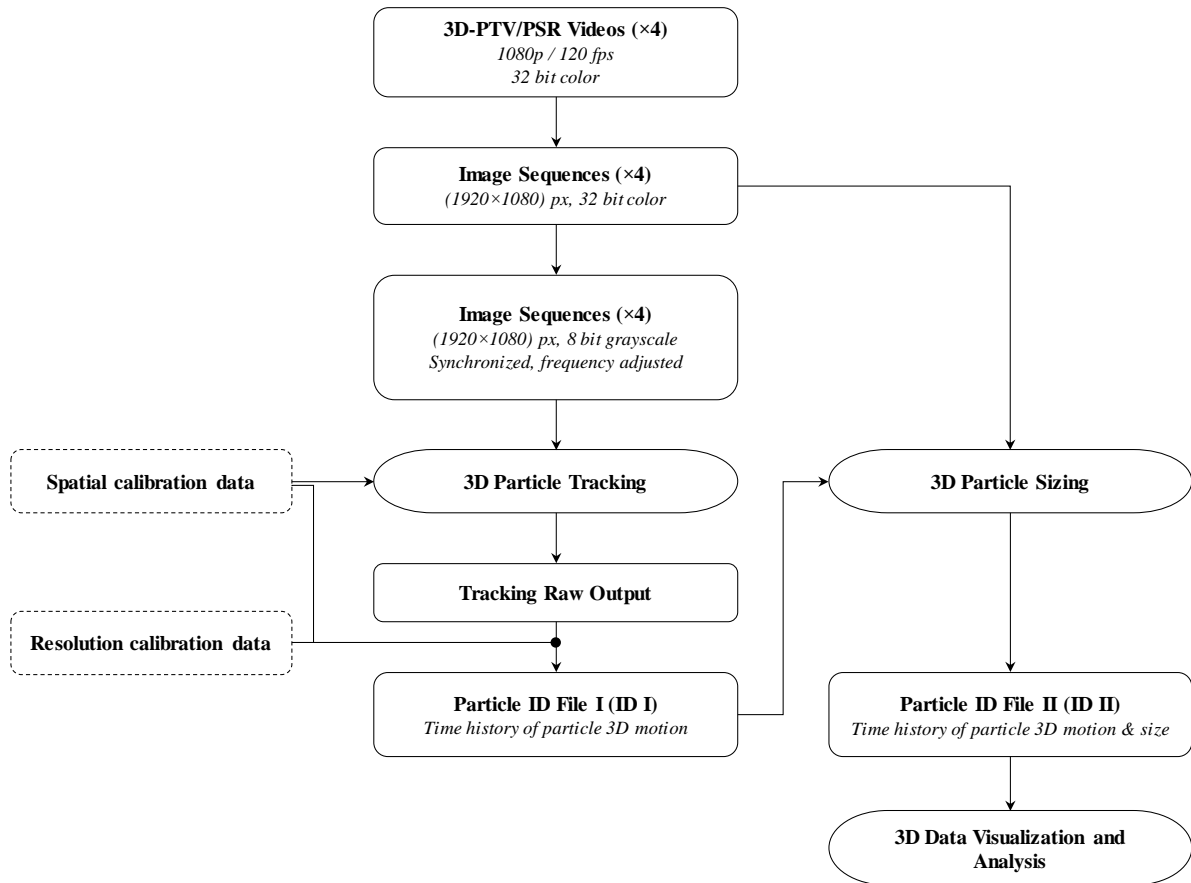
Fig. 6. System processing flowchart.

The system processing flowchart is shown in Fig. 6. Videos acquired by the 3D-PTV/PSR system are rendered into image sequences ((1920×1080) px, 32-bit color) by extracting individual video frames (unaltered) via a commercial software. Image sequences are then synchronized and transposed into grayscale color space (8-bit) using an in-house MATLAB code. If necessary, the code allows for sequence downsampling to reduce computational burden for the 3D tracking step, should the motion of observed particles be too highly resolved. Grayscale image sequences are then processed by the PTV software [54], in conjunction with the spatial calibration data (see details in Sec. 2.3.2). An in-house FORTRAN code generates individual particle "identity" files (ID I) that gather time-stamped particle

14

motion characteristics from the raw outputs of the PTV software. Among others, ID I files include: the video frame number and corresponding time step, the particle 3D coordinates in object space and the particle 2D coordinates in all image spaces (four views). The code also computes particle velocities based on the previous and current particle locations, as well as quantities related to the particle sizing step (distance D and local resolution R^* – see definitions in Sec. 2.4.2), which requires both spatial and resolution calibration data. The color image sequences and selected data from ID I files (particle image 2D coordinates, particle 3D coordinates and resolutions R_i^* 's) are then used for particle sizing purposes. A MATLAB code has been developed to re-construct particle models in 3D from which size, volume, orientations, etc. can be extracted. Further details about the sizing methodology are given in Sec. 2.4. Particle tracking and sizing results are compiled in particle ID files II (ID II) that are used for 3D data visualization and analysis.

2.3. Firebrand tracking using 3D Particle Tracking Velocimetry (3D-PTV)

2.3.1. Methodology

The 3D tracking of firebrands is computed via the open-source software OpenPTV [54]. It is used to perform the following set of operations, some of which were previously highlighted in Sec. 2.1: (1) Calibration of the multi-camera system (see details below); (2) Detection of the particles: firebrands 2D image coordinates are found using a pixel intensity-weighted centroid operator; (3) Particle correspondences across multi-camera views using the epipolar line intersection technique; (4) Computation of 3D particle coordinates in the object space; and (5) Particle tracking via spatio-temporal particle matching using both image and object space information. Further details about these steps can be found in the work of Maas et al. [34, 51] and Wilneff [52].

2.3.2. Spatial calibration for 3D firebrand tracking

(a)   (b)
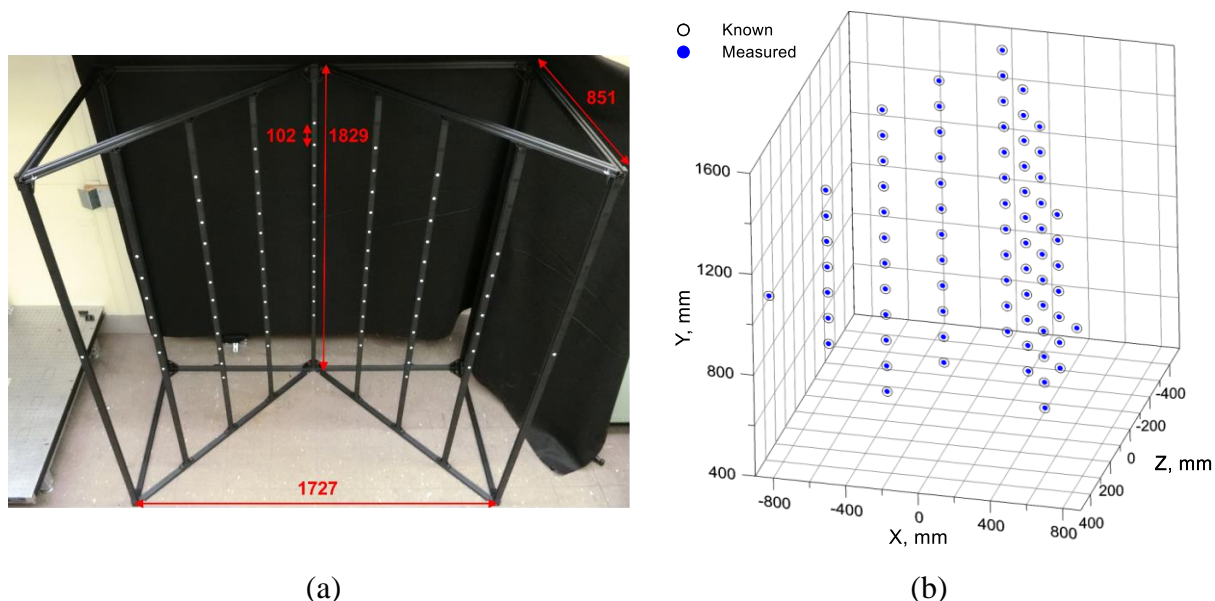
Fig. 7. 3D spatial calibration target: (a) photograph with dimensions (in mm); (b) verification test: known 3D coordinates of target points vs. measured target point positions after calibration.

The spatial calibration is performed by imaging a 3D V-shaped target encompassing the control volume of interest. The target, shown in Fig. 7a, contains 76 dots with known 3D coordinates, all being visible from the four viewpoints. Calibration images are processed by the 3D-PTV software [54] using a mathematical model of spatial resection [52] to yield both internal and external camera orientation parameters. A verification test is systematically performed after calibration by processing original target images and comparing known and measured target point positions (example shown in Fig. 7b). Hence, the expanded uncertainty in position can be estimated and is typically on the order of ± 1.5 mm in all directions.

2.3.3. Tracking efficiency and trajectory recombination strategy
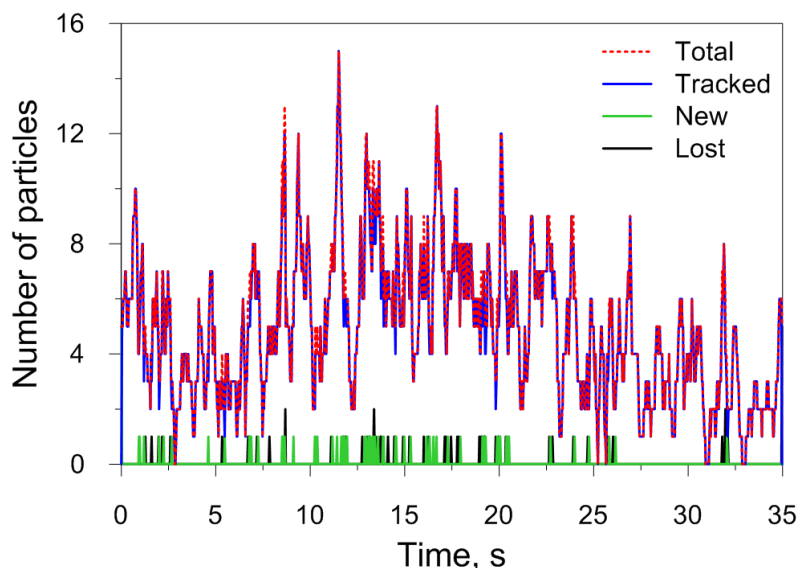
Fig. 8. Illustration of tracking efficiency monitoring (Test volume: X = (-600 to 600) mm, Y = (600 to 1400) mm, and Z = (-300 to 300) mm). Data is from experimental case discussed in Sec. 4 (combusting cuboids). Increase/decrease of the total and tracked number of particles in absence of new or lost particle events (see for instance, 27 s < *t* < 30 s) is due to arrival/departure of particles in/from the test volume.

The tracking efficiency can be qualitatively estimated by monitoring, at each timestep, the total number of particles successfully located in 3D, within a judiciously chosen test volume[2]. This number encompasses particles belonging to the three following categories: (1) "Tracked" particle: a particle identified before and after the current timestep; (2) "New" particle: a particle identified for the first time in the current timestep; and (3) "Lost" particle: a particle not identified beyond the current timestep. For illustration purposes, Fig. 8 shows a graphical representation of the number of particles in each category for the experimental case presented in Sec. 4 (combusting cuboids). In this case, the close match between the total and tracked particle numbers indicates good tracking efficiency. Systematically performing such verification was found to be a good practice throughout this work since it provides, to some

---

[2] The test volume should be defined well within the system control volume to avoid accounting for particle appearance/disappearance events near the control volume boundaries. Efficient tracking implies that a particle is recognized and properly tracked at all times while present in the test volume.

16

extent, a guidance for the choice of optimal parameters while configuring both particle detection and tracking steps as previously described. Figure 8 also shows that there are some seldom occurrences of "new" and "lost" particles, and these are usually associated with the following type of particle trajectory:

(1) Spurious trajectory: this is an unwanted trajectory lasting very few time steps (with very small averaged displacement) usually due to secondary tracked object (e.g., a landed firebrand, a bright element in the background, etc.). This trajectory is typically filtered out prior to any particle tracking/sizing analysis using an operator based on the mean particle displacement. In rare occasions, it might remain if the operator is set to include very slow (small) firebrands;

(2) Incomplete/shortened trajectory: this is a valid trajectory with a late start/early ending within the measurement volume. The few missing steps might be due to a lack of particle visibility. This type of trajectory can be processed in the same manner single (full length) trajectories are, despite the missing information.

(3) Broken trajectory: this is a valid portion of a particle trajectory, for which at least one trajectory correspondence can be found within the measurement volume. Correspondences between sister trajectories are not known a priori.

Among these, broken trajectories require attention since each portion of a particle trajectory would be, by default, attributed to a new particle. This could be an issue when performing size distribution analyses, since a single particle could be counted multiple times, and sizing data from sister trajectories would not be merged. To circumvent the issue, an algorithm is used to detect and recombine broken trajectories. Figure 9 illustrates the recombination process. Within a specified volume, the algorithm monitors "Early-Ended" (EE) and "Late-Started" (LS) particle trajectories. Each EE occurrence is provided with a list of LS candidates. All candidates' starting points are to happen in a temporal search window (gray areas in Fig. 9): (1) that directly follows the end of the EE trajectory, and (2) whose duration is limited. This duration is user-specified and may be adjusted depending on the problem considered (6 timesteps in the present case). A linear best fit procedure [55] applied to the EE trajectory data points is used to predict the X, Y and Z particle positions versus time throughout the allowed search window. The first and second data points of the LS trajectory candidates are then compared to their predicted values. If both set of points fall within user-specified tolerance bands (shown in Fig. 9 by the vertical errors bars – see additional details in caption) in all directions, then the EE and LS candidate trajectories are considered matched. As an example, Table 3 gives an overview of the recombination efficiency for the dataset presented in Sec. 4 (combusting cuboids). In this case, the algorithm allows to recombine up to 90 % (87 out of 97 total) of all broken trajectories. This recombination strategy is applied when performing the firebrand 3D sizing analysis presented in Sec. 4.2.3.
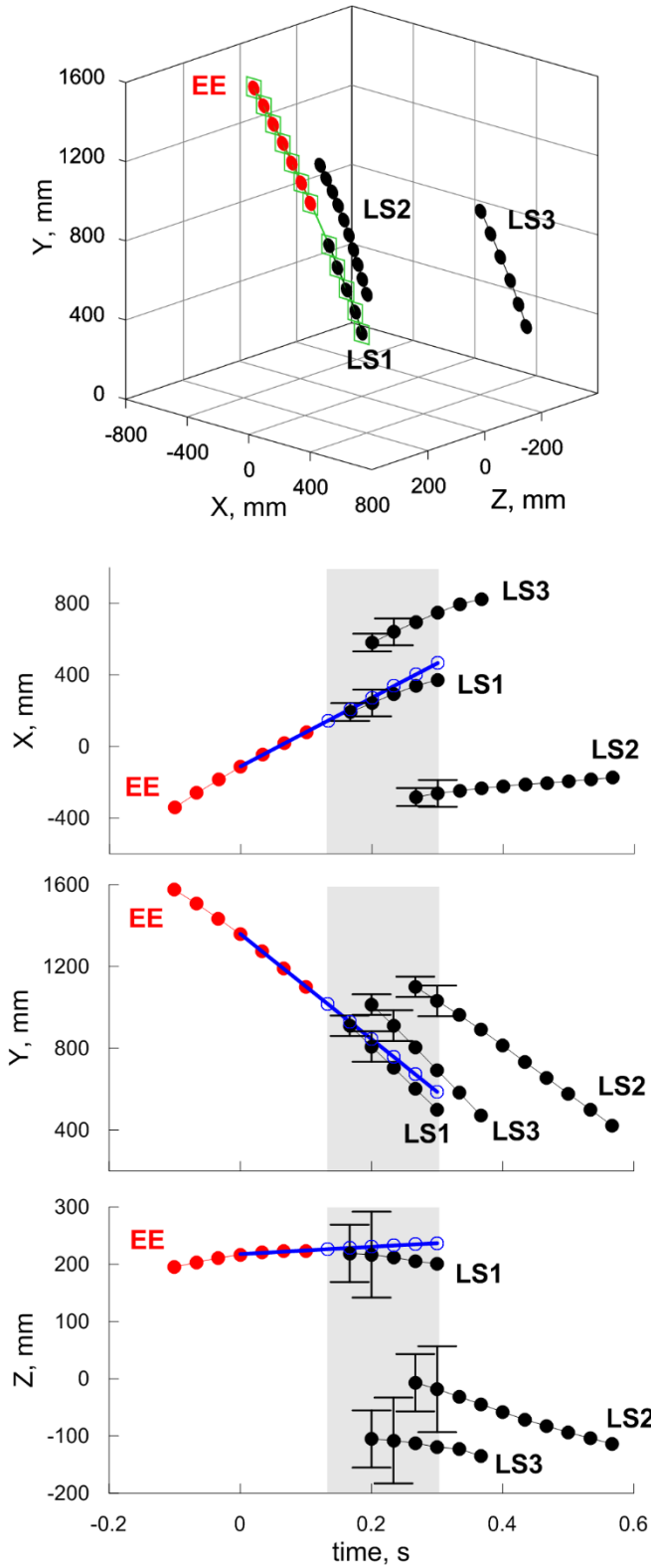
Fig. 9. Illustration of the operations performed by the algorithm for matching broken trajectories (red dots: "early ended" (EE) trajectory, black dots: "late-started" (LS) trajectories, green open squares: reconstructed trajectory, blue open dots: particle position predictions based on a linear best fit performed on the last four data points of the EE trajectory (blue line), grayed area: user-defined temporal search window. Vertical error bars display the allowed tolerances for matching predictions to actual LS particle positions. In the present case, the tolerance τ is ± 50 mm for the first data point and $c \times \tau = 75$ mm for the second data point, with $c = 1.5$ a relaxation factor).

Table 3 Overview of the numbers of particle trajectory by type for the test case presented in Sec. 4 (combusting cuboids) after proceeding to trajectory recombination.

Trajectory types	% (# of trajectories)
Spurious	0.15 (1)
Singles	85.8 (593)
Broken	
Successfully recombined	12.6 (87)
Not recombined	1.45 (10)
Total	100 (691)

2.4. Firebrand sizing via 3D Particle Shape Reconstruction (3D-PSR).

The sizing of airborne firebrands presents a challenge due to the variation of particle projected shapes (a.k.a. "silhouette") depending on the viewpoint considered. Simply extracting averaged size/surface area information based on the different 2D views does not produce satisfactory results in terms of describing the true size and shape of complex particles. This limitation is inflated as a particle moves through the control volume since it may tumble and change its orientation with respect to the camera planes, therefore introducing a time dependence in the silhouette characterization. In the present work, a more robust sizing approach was developed: each particle is reconstructed in 3D using combined views of the multi-camera system, following the principles of the Visual Hull concept [43]. Such a reconstruction incorporates information from the 3D-PTV analysis, including camera orientations, as well as particle coordinates in both 2D image and 3D object spaces. Additionally, a calibration must be performed to determine the image resolution as a function of particle 3D position for each camera (necessary input for the accurate representation of the particle boundaries when transposed into the object space). Ultimately, the size characteristics of a particle are extracted using a series of the 3D models obtained at all relevant timesteps (typically ≈ 10 models).

2.4.1. Methodology

The 3D shape reconstruction of a particle includes the following steps:

(1) Edge detection; the set of particle 2D image coordinates is retrieved from the 3D-PTV output and is used to locate the particle across the four views and perform a multi-step particle boundary detection using the corresponding silhouettes; the boundary detection method follows an unsupervised threshold selection for picture segmentation [56] and therefore does not require any user input.

(2) 3D shape reconstruction; the reconstruction process is illustrated in Fig. 10. Particle boundaries obtained from the previous step are translated to the known 3D location of the particle in the object space[3] and rescaled according to the resolution calibration function to yield their true size (see next paragraph). Projection cones, whose apexes are defined by the

---

[3] The 2D centroid positions relative to the particle boundaries are preserved and matched with the 3D particle location. All coordinates are results of the 3D-PTV output.

camera perspective centers and profiles set by convex envelopes formed around the new particle boundaries[4] in the object space, are created (Fig. 10a). The volume defined by the intersection of the four cones represents the 3D shape of the particle (Fig. 10b). A 3D model of the particle can be reconstructed by randomly generating points within a localized search box containing the volume of intersection and retaining only those belonging to the latter. The resulting cloud of data points defines the particle convex hull, and the shell formed by the outermost points can be saved and used for sizing purposes.

(a)   (b)
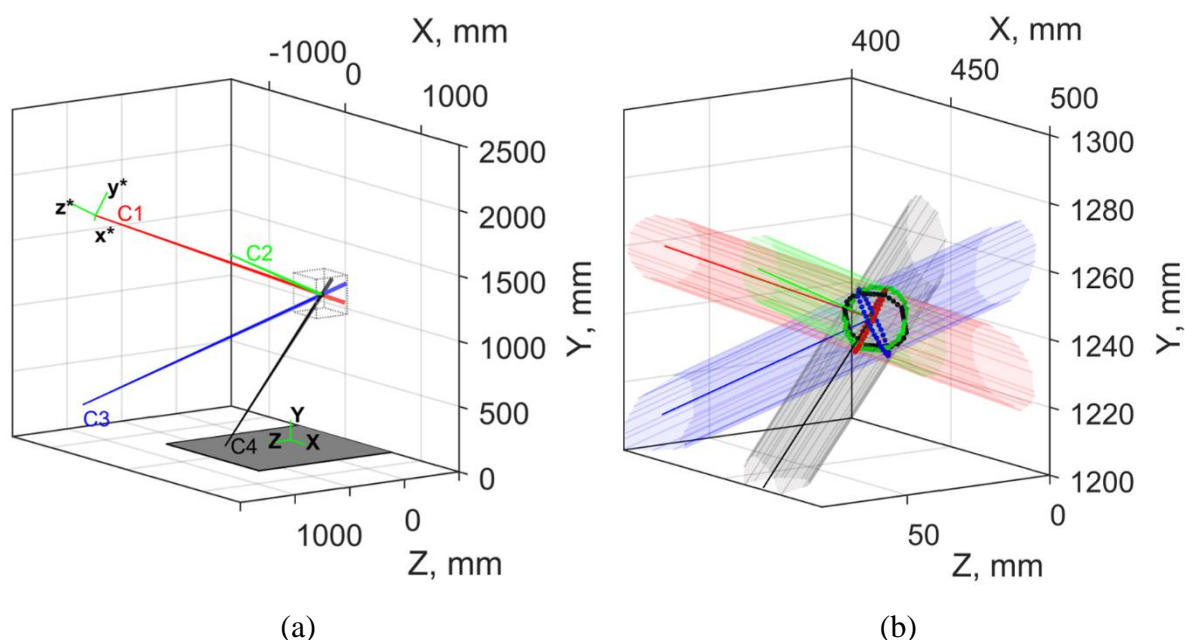
Fig. 10. Illustration of the 3D particle shape reconstruction process: (a) macroscopic view of the workspaces and transformations, (b) Zoom on the cone intersection area contained in the gray square shown in Fig. (a).

Because of the stochastic nature of orientations of airborne firebrands and given the fact that the present camera arrangement is fixed, it is highly desirable, when performing sizing operations on a firebrand, to use as many 3D reconstructions as possible (i.e., run a combined analysis of all available convex hulls for each individual particle). After performing step 1 and 2 for all timesteps when the particle appeared, principal component analysis is used to identify the main axis of the resulting point clouds and re-orient them accordingly. Scatter plots of the particle contours can be created by performing orthogonal projections of the data points located on the outer boundaries of each individual hull, for each orthogonal view considered. The outline projection is illustrated in Fig. 11a for a single timestep reconstruction. Figure 11b shows cumulative plots with all available outlines from which sizing characteristics can be extracted (e.g., averaged particle height, width, etc.). Although obvious, it is important to stress that the accuracy of the particle sizing step is closely related to that of the Visual Hull reconstruction technique, which itself depends on a broad range of factors. Some of these factors are known by the user, e.g., the number of cameras, their arrangement and the spatial

---

[4] These convex envelopes can be visualized as the shapes that rubber bands would take if wrapped around the new particle boundaries. This simplification greatly improves the problem computational tractability.

resolution achieved, while others are particle specific and therefore unknown a priori, e.g., the particle shape, size, orientation and location/flightpath within the system control volume. Hence, a sizing accuracy cannot be expressed based on the knowledge of the experimental layout alone, although computational strategies to gain insight into detailed measurement accuracy could be explored (see related discussion in Sec. 5).

(a)   (b)
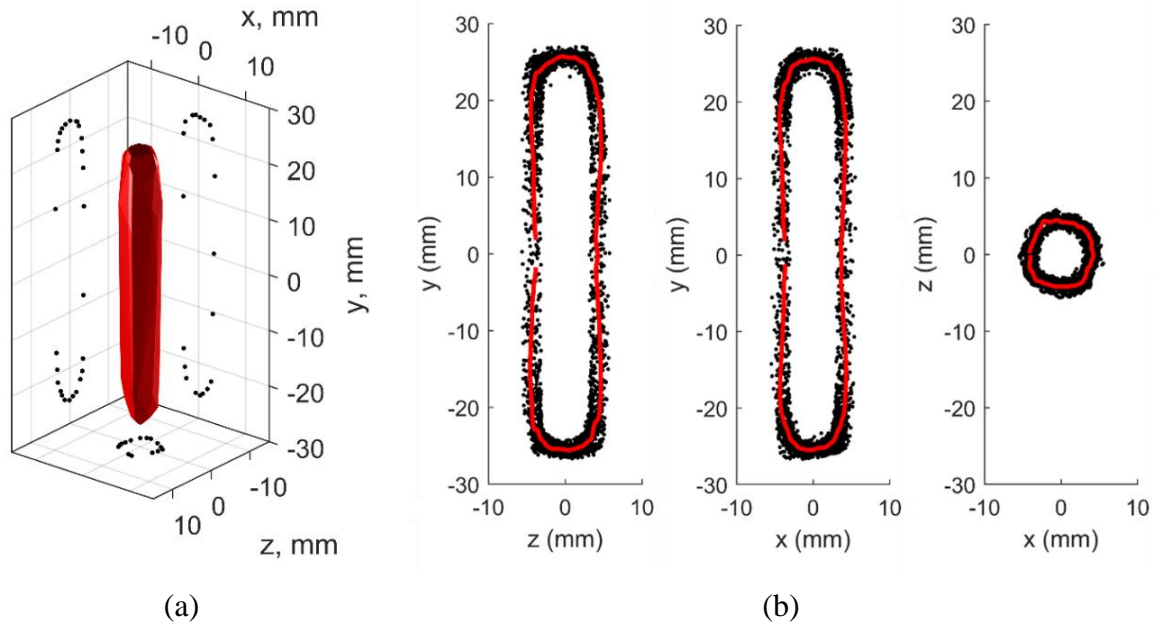
Fig. 11. Illustration of: (a) extraction of outlines from a 3D particle model (single timestep); (b) cumulative particle outline plots (all timesteps included). The red line indicates the average particle contour.

2.4.2. Local resolution calibration for 3D firebrand reconstruction

As previously mentioned, an important requirement of the 3D particle reconstruction is the knowledge of the spatial resolution versus 3D position across the control volume. This knowledge is acquired by calibrating the multi-camera system with a dedicated target. The target is composed of 6 white spheres ($\varnothing = 25.4$ mm) vertically distributed along a 1.7 m long pole with a separation distance of 224 mm. The pole is moved at 22 different locations within the control volume, and images of the target are recorded each time from the four viewpoints. An image processing algorithm is then used to isolate each individual sphere and evaluate its characteristic dimensions. To avoid complexities arising from eccentricity in the image measurement of spherical targets [50, 57], the sphere boundaries are treated as ellipses and their minor axis length (in pixels) is retained as their characteristic projected size. For the largest sphere image considered (≈ 46 pixels) and widest view angle possible ($\approx 37°$), the maximum deviation from the theoretical projected size does not exceed ½ a pixel. The sphere image sizes, actual sphere size, and known sphere coordinates can be used to generate 3D maps of local resolution (R^*, in mm/pixel) for each camera. An example of such a map is given in Fig. 12a for Camera #1. The data shown in Fig. 12a can be scaled introducing the distance D of any target point (X, Y, Z) to a reference plane containing the camera perspective center O and parallel to the image plane. Therefore, D can be expressed as:

$$D = |aX + bY + cZ + d| \tag{6}$$

with a, b and c, the coordinates of the normal $\boldsymbol{n}$ to the reference plane (calculated using Eqs. 2 and 3):

$$\boldsymbol{n} = \begin{bmatrix} a \\ b \\ c \end{bmatrix} = \begin{bmatrix} r_{21}r_{32} - r_{31}r_{22} \\ r_{31}r_{12} - r_{11}r_{32} \\ r_{11}r_{22} - r_{21}r_{12} \end{bmatrix} \tag{7}$$

and:

$$d = -(aX_0 + bY_0 + cZ_0) \tag{8}$$

It is seen in Fig. 12b that the scaled dataset collapses onto a straight line whose equation can be easily implemented in the particle sizing code. Given this calibration methodology, the primary source of uncertainty for the resolutions comes from the accuracy in identifying the spherical targets edges which is typically performed at a $\pm$ 1 pixel confidence level (the corresponding iso-lines are shown in blue in Fig. 12b). Hence, the uncertainty depends on the 3D position of the target point considered and is at most 0.1 mm/pixel for points located the farthest away ($\approx$ 2.4 m) from the camera image planes.

(a)   (b)
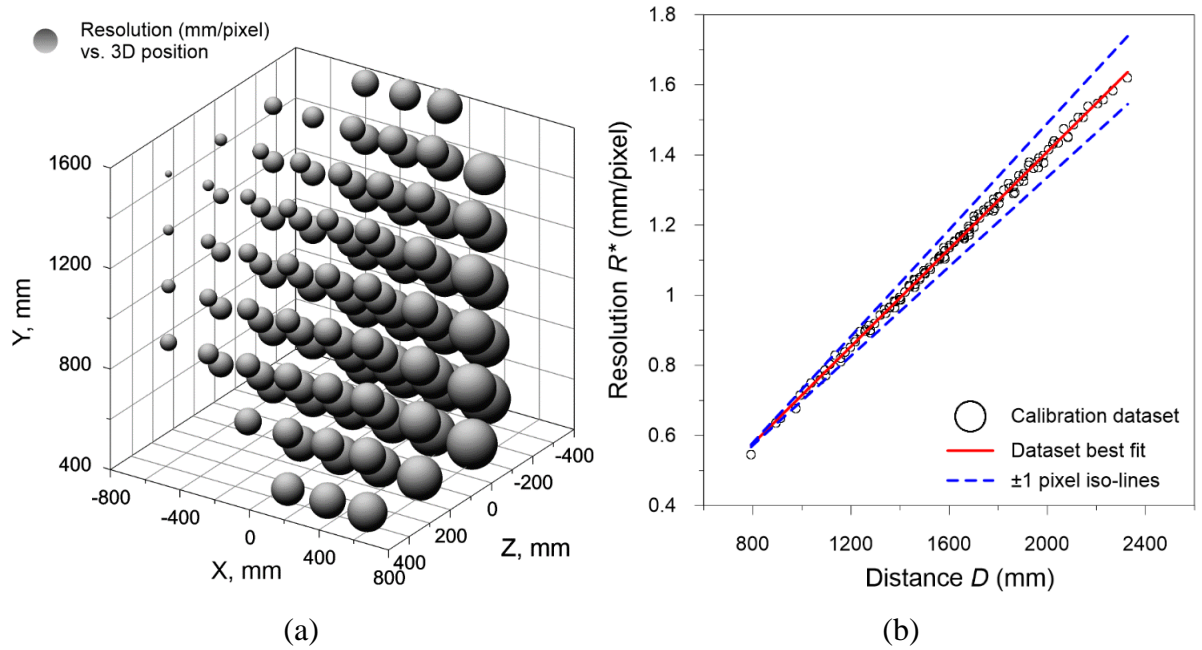
Fig. 12. Mapping of spatial resolution: (a) vs. 3D location in the control volume (bubble diameter is proportional to actual resolution in mm/pixel, data is for Camera #1), (b) vs. scaling distance D.

3. Application to model firebrands in laboratory settings: validation cases

The system described in the previous sections has been tested in a series of validation experiments using combusting (model embers) and non-combusting (white particles) objects.

The following sections are meant to give an overview of typical tests performed to assess proper implementation of the 3D tracking and sizing techniques.

3.1. Rotating firebrand stick

Proper 3D tracking is verified by monitoring the motion of a rotating punk stick, whose glowing lit end serves as model firebrand. The setup is shown in Fig. 13. The punk stick (53.5 mm exposed length, ≈ 3.6 mm thick) is attached to a metallic arm (397 mm axis-to-axis separation distance), itself mounted on the shaft of a gear box motor controlled by a DC power supply. The centerline of the motor shaft is set to coincide with the origin of the global coordinate system in the xz plane. After lighting the end of the stick, the angular velocity is increased, and several rotations are observed until steady glowing is obtained. Data is then acquired at 120 Hz during a set of two complete revolutions and sampled down to 12 Hz prior to processing (total of 136 individual datapoints). The 3D-PTV measurements are compared to the predicted trajectory of the model ember which is inferred from the known dimensions in the experimental layout, defining the center of the model firebrand at mid height of the glowing spot (its length slightly varies depending on the stick direction of motion with respect to the camera observation plane but is taken to be constant and equal to 24.7 mm for simplification). The prediction assumes that the tip of the stick describes a circular motion contained in a single xz plane. In practice, the predicted trajectory encapsulates some level of uncertainty, likely on the order of ± 5 mm in all directions, given unavoidable alignment errors due to the rather large observation volume considered, and the assumption of a "particle" centroid positioned at constant height.
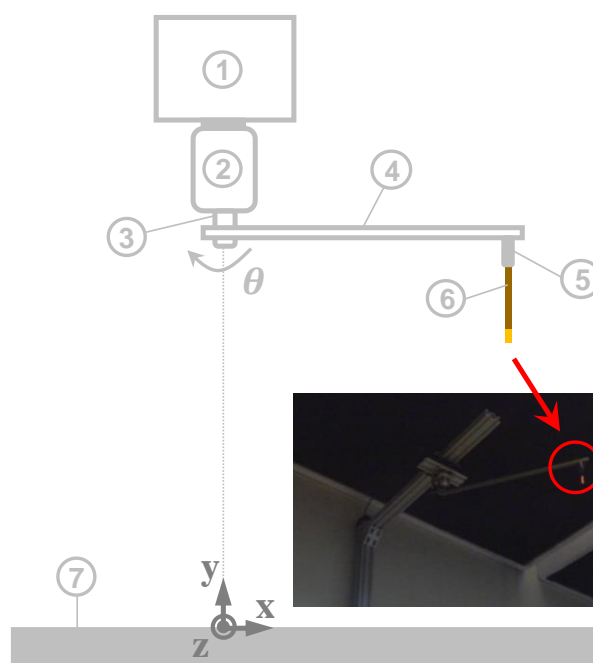
Fig. 13. Schematic representation of the rotating stick setup for tracking validation: (1) Motor attachment arm; (2) Gear box motor; (3) Motor shaft; (4) Rotating arm; (5) Stick holder; (6) Lit punk stick; (7) Optical table. The insert shows a picture of the actual setup taken with Camera #3.

The measured and predicted trajectory of the model firebrand are shown in Fig. 14a. Overall, the agreement is found to be very good, with a measured radius and height of 396.2 mm ± 2.3 mm and 1526.9 mm ± 3.7 mm compared to the predicted values of 396.9 mm and 1523.3 mm, respectively. Measured instantaneous velocities of the model ember are compared to the predicted average over two turns in Fig. 14b. There is an excellent agreement between the measurement average (44.3 cm s^{-1} ± 1.9 cm s^{-1}) and the predicted value (44.3 cm s^{-1}). The slight periodical variations of the instantaneous measurements (around the constant predicted value) are true occurrences and are likely to be due to imperfections in the rotating system (load/motor inertia match, system not perfectly rigid, etc.).
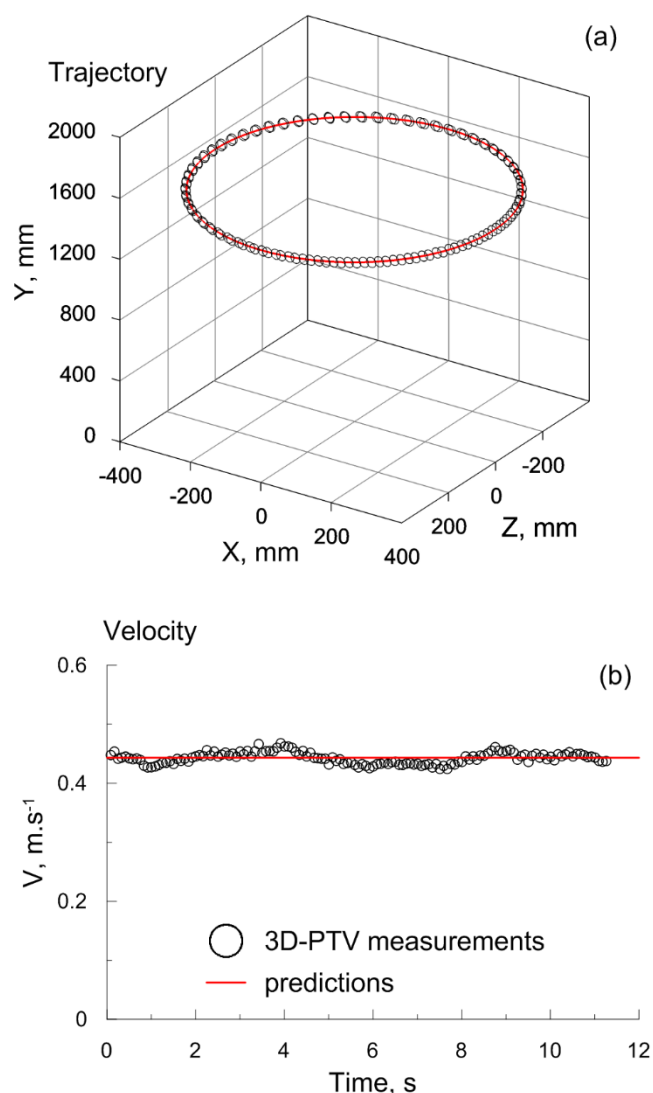
Fig. 14. 3D-PTV measurements vs. predictions: (a) 3D trajectory and (b) velocity of end of lit punk stick. Predictions refer to the actual path of the model firebrand (which can be inferred initially from the known layout of all experimental components) and the calculated average velocity over two turns, respectively.

3.2. Vertical release of spherical particles

A total number of 110 quasi-spherical particles were randomly released in space and time from a platform (50.8 cm × 76.2 cm) fitted with 19 equally distributed 16 mm diameter holes. The platform is located ≈ 1.65 m above the optical table (see Fig. 15). The particle set included the following size classes (the particle count and effective diameter are provided between parenthesis): 6 mm (38, 6.2 mm ± 0.2 mm), 8 mm (36, 7.9 mm ± 0.3 mm), 10 mm (13, 9.9 mm ± 0.2 mm), 12 mm (10, 11.9 mm ± 0.2 mm), and 14 mm (13, 13.8 mm ± 0.4 mm). These classes essentially belong to the lower end of the particle size spectrum that can be investigated by the system described in Sec. 2. The size classes are specifically chosen in close proximity to provide stringent testing conditions and demonstrate the system ability to achieve fine size classification. Falling spheres were tracked and sized according to the methodologies detailed in Sec. 2.
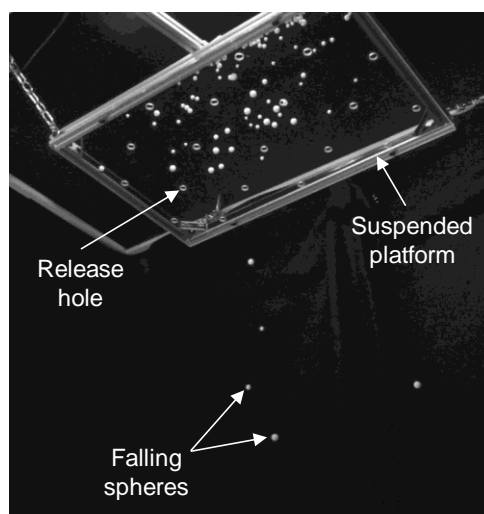
Fig. 15. Setup for the particle sizing validation experiment (annotated cropped view from Camera # 4).

Size distribution histograms are shown in Fig. 16a. Datasets for both measured ("Airborne" in white) and known ("Sphere diam." in black) sizes are compared (overlap shown in gray). Measurements taken along the z and x axes are similar and agree relatively well with the known sphere diameters. Note that a perfect match between the two datasets is not to be expected given that the chosen class width (2 mm) is on the order of the smallest resolution achieved (see Fig. 12b, ≈ 1.6 mm/pixel in the back of the control volume) and that the unit area for particle silhouette detection is 1 pixel. In the present case, it was noticed that, depending on the view considered, nonuniform sphere surface area illumination could slightly bias the contour detection towards the inner silhouette boundaries (i.e., -1 pixel as compared to visual observations), which in turn explains the observed shifts towards the smaller size classes. On the other hand, some of the measurements taken along the *y*-axis fall in size classes that are well beyond the maximum sphere diameter. These overestimations are the result of a nonsystematic artifact of the Visual Hull reconstruction: given a particle property (shape, size, orientation and location within the control volume) and system layout (finite number of cameras, cameras location in space), blind volumes, not carved by the silhouette projection

25

cones, might remain and contribute to the artificial enlargement of the particle. This is illustrated in Fig. 16b where a 3D reconstruction "worst case scenario" is presented for a 14 mm sphere bringing a contribution to the 20 mm class count of the *Airborne y* dataset. Added volumes in the front (low *y*) and back (high *y*) of the visual hull are clearly seen by comparing both known (blue) and reconstructed (red) sphere shapes. Similar observations were reported by Kleinkort et al. [48] for a three- and a five-camera system.

(a)   (b)
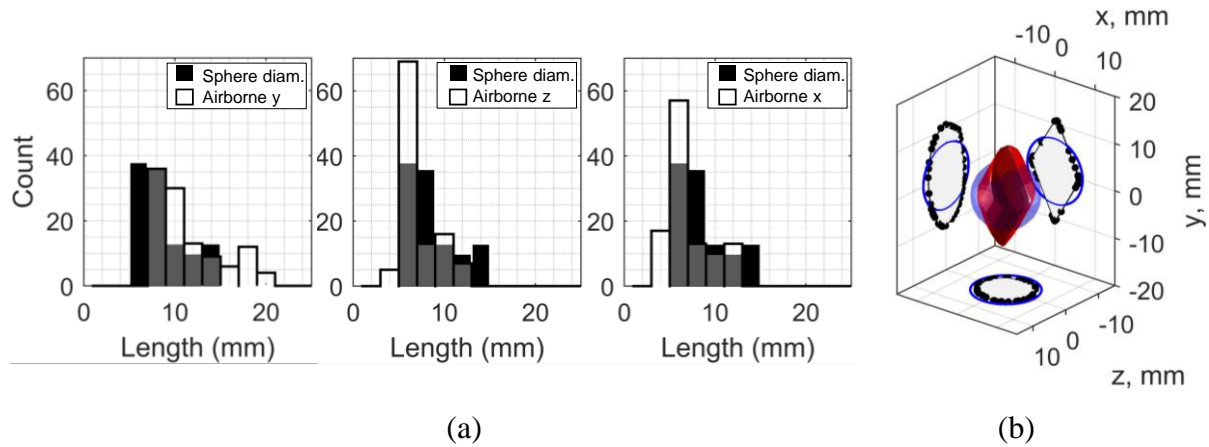
Fig. 16. Size distribution comparison: (a) known sphere sizes (*Sphere diam.*) versus measurements (*Airborne*) along the particle *y*, *z* and *x* axes, respectively (All axes mentioned are local to the re-oriented particle, size distribution overlaps are shown in gray); (b) Example of a 3D reconstructed sphere shape and its projected boundaries (in red, single time step) contributing to the 20 mm size class observed in the "Airborne y" histogram. Actual sphere shape and its projected boundaries are shown in blue.
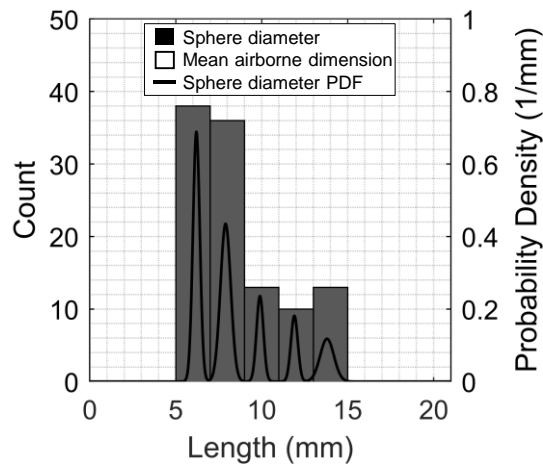
Fig. 17. Size distribution comparison: known sphere sizes (*Sphere diameter*) versus mean of the measured sizes along the *x*, *y* and *z* axes (*Mean airborne dimension*). All axes mentioned are local to the re-oriented particle. Histogram overlap is shown in gray. Sphere diameter PDF based on caliper measurements are superimposed (black lines, right vertical axis).

Despite the limitations mentioned above, Fig. 17 shows that an exact sphere size classification can be achieved based on the mean of the measurements along the x, y and z axes. Strategies to improve the current sizing approach, especially improving the Visual Hull reconstruction fidelity, are further discussed in Sec. 5.

4. Application to an artificially generated firebrand shower

4.1. Experimental layout and procedure

The emberometer was tested at the NIST National Fire Research Laboratory (NFRL). The experimental layout and procedure, similar to those described in Ref. [53], are further detailed below. The emberometer was set downstream of a firebrand generator, following the arrangement shown in Fig. 18a. The generator, designed according to some of the specifications given in Ref. [58], is operated to produce firebrand "showers" whose particle number densities are visually consistent with field observations. The firebrand generator is made of a centrifugal blower (*Cincinnati Fan PB-9*) connected in line with cylindrical stainless-steel duct elements (149 mm I.D.). Additional details regarding the duct assembly, including the fuel load location and key dimensions, are provided in Fig. 18b. In the present case, the fuel was made of Douglas fir cuboids (side lengths: 7.8 mm, 8.1 mm, and 12.9 mm, ± 0.4 mm). The fuel moisture content was measured with a handheld moisture meter (*Delmhorst J-2000*) and was confirmed to be less than 6 %.

(a)   (b)
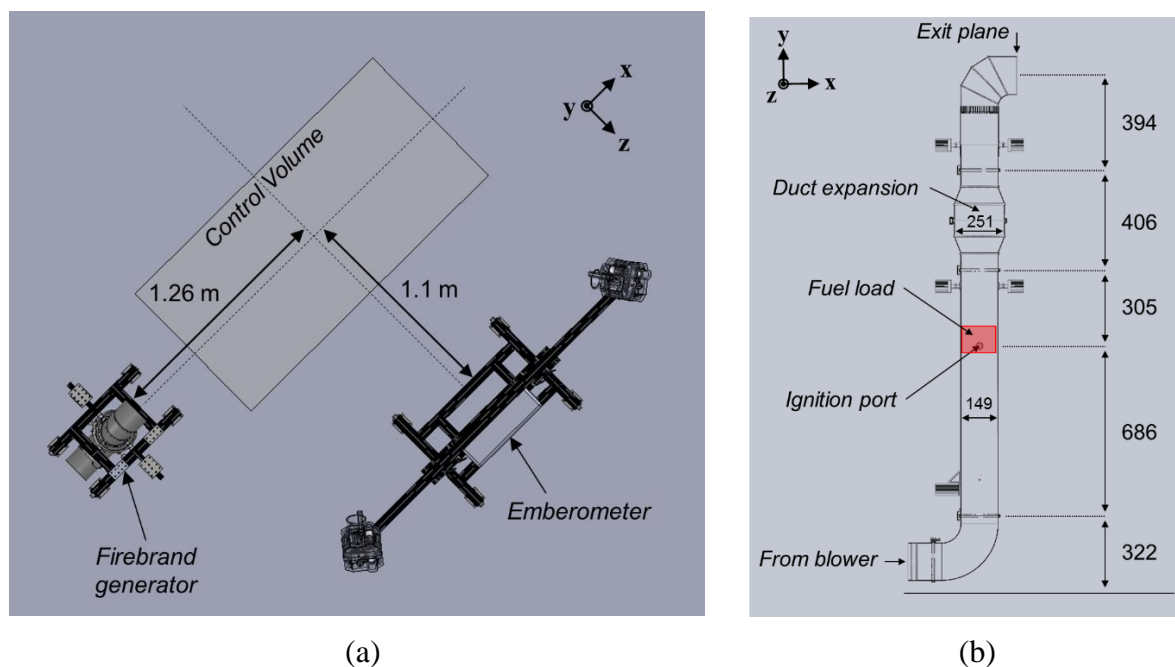
Fig. 18. Experimental layout for NFRL tests: (a) Top view of test setup, (b) Cross-sectional view of firebrand generator duct assembly (all dimensions in mm).

The test with firebrands was run as follows: (1) 350 g ± 1 g of pristine fuel was introduced in the firebrand generator (see Fig. 19a); (2) the blower speed was set to 5 Hz and two propane torches (*Bernzomatic TS8000*) were ignited and inserted slightly below the fuel batch, on opposite sides. Ignition was maintained for 45 s; and (3) After 45 s, the propane delivery was

27

stopped, and the blower speed was set to 20 Hz. Shortly after the blower speed adjustment, a large flame settled at the generator output. The flame length slowly decreased until complete flame disappearance after ≈ 48 s. The first firebrands were produced ≈ 16 s after the flame onset, and generation continued for about 74 s. The analysis presented in the next section concentrates on a 35 s time window (beginning 38 s after the flame onset), when the peak production of firebrands occurred. Most landing firebrands were collected in aluminum pans filled with water covering an area of about 2.4 m^2 and starting 0.56 m downstream of the firebrand generator exit plane. Collected firebrands (999 count) were dried and their sizes measured to provide an independent dataset for firebrand size distribution comparison. An example of a cold ember image used for the 2D size analysis is provided in Fig. 19b.

| (a) | (b) |

Fig. 19. Firebrands: (a) pristine fuel batch loaded in firebrand generator vs. (b) cold firebrands collected for 2D image size analysis (the multicolor bounding boxes are used to extract 2D ember dimensions).

4.2. Results

4.2.1. Firebrand 3D tracking and firebrand flux metric development

Figure 20 shows an example of the four-camera views at t = 8.375 s. Particles tracked in the current timestep are circled in red and their trajectories (in each 2D image plane) are shown by the blue lines using tracking information computed during the previous timesteps. Although more complex to implement than the "classic" stereoscopic setup, the quad-view approach chosen in the present work is particularly suited to the firebrand problem: firebrand visibility might vary significantly depending on the imaging angle (e.g., background interference), therefore multiple views are highly desirable to ensure robust particle tracking. This is illustrated in Fig. 20 where the trajectory of Particle #145 is found to be incomplete in the image plane of Camera #1. This lack of information has no impact on the successful reconstruction of its 3D trajectory since the information is not lacking in the other image planes (hence photogrammetry principles, as described in Sec. 2.1, can be successfully applied). Note that non-circled firebrands seen close to the firebrand generator exit on the camera view #4 have not entered the system control volume yet and are therefore not tracked.

28
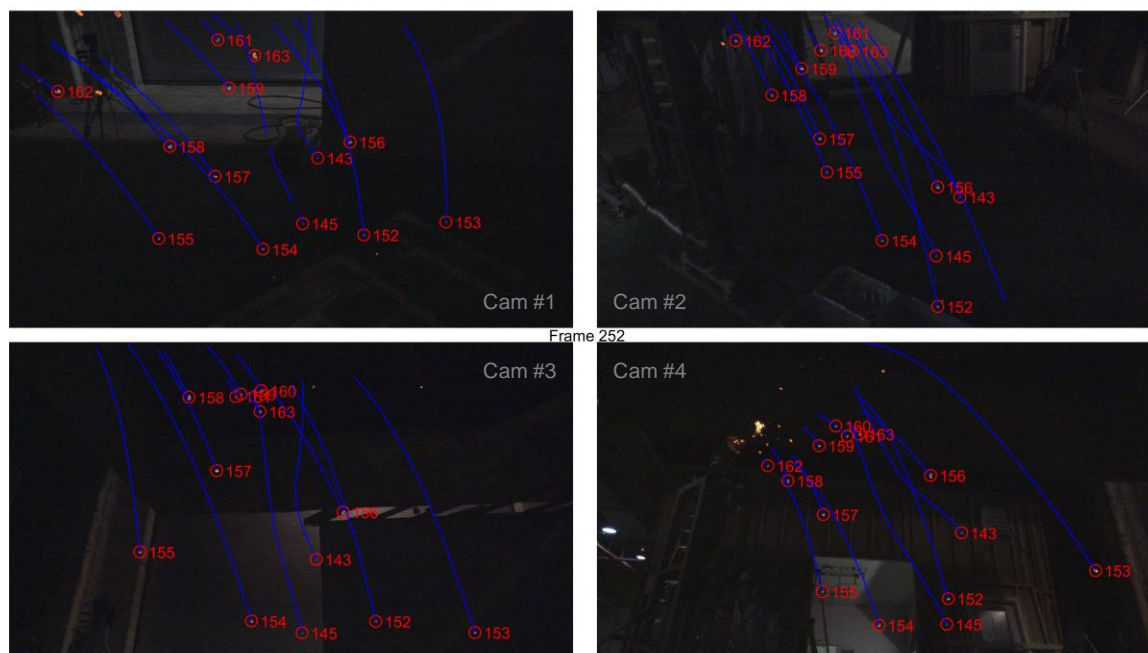
Fig. 20 Example of the quad view during operations (t = 8.375 s) with data processing overlays: red circles and numbers: firebrand identifiers, blue lines: firebrand trajectories in each image plane. Top left and right views taken from Camera #1 and #2, bottom left and right views from Camera #3 and #4, respectively.

Fig. 21a shows a cumulated plot of 691 3D trajectories reconstructed in the present case. The system allows for the characterization of a wide range of firebrand dynamics, including low-velocity motion (< 0.4 m s^{-1}) of small embers (air draft/lift force sensitive) as well as projectile-like motion (> 4 m s^{-1}) of gravity-driven embers. An example of both types of trajectories and velocity magnitudes is given in Fig. 21b.

The firebrand exposure can be quantified by monitoring the number of particles crossing a reference surface of defined geometry and location within the experimental control volume, therefore yielding a Cumulative Particle Count (CPC, unit: particles m^{-2}). In the present case, the reference surface is a disk, whose center is located at X = -150 mm, Y = 1000 mm, and Z = 0 mm and with a radius r equal to 200 mm (see Fig. 21a). Both location and size of the reference surface are carefully chosen so that the characterization stays representative of the exposure conditions met in the core flow. Figure 22 shows the CPC versus time given the reference surface. The total CPC over the test period is close to 1281 particles m^{-2}. The CPC time-resolved data can be used to derive the corresponding Particle Number Flux (PNF, unit: particles m^{-2} s^{-1}), which represents a number of particles per unit surface area, per unit time. It can be seen in Fig. 22 that the PNF peaks up to 111.3 particles m^{-2} s^{-1} at t = 9 s, most values being within the 25-65 particles m^{-2} s^{-1} range throughout the test. At this point, it is important to recognize that both CPC and PNF distributions, such as reported in Fig. 22, depend on the reference surface orientation and that the firebrand exposure perceived in the core flow cannot be fully characterized on the basis of a single surface orientation. As an example, a fictitious case, for which the firebrand flow is identical to the one described above, but with additional firebrands with trajectories parallel to the reference surface shown in

29

Fig. 21a, would yield identical CPC and PNF distributions, despite obviously different exposure levels.

(a)

(b)
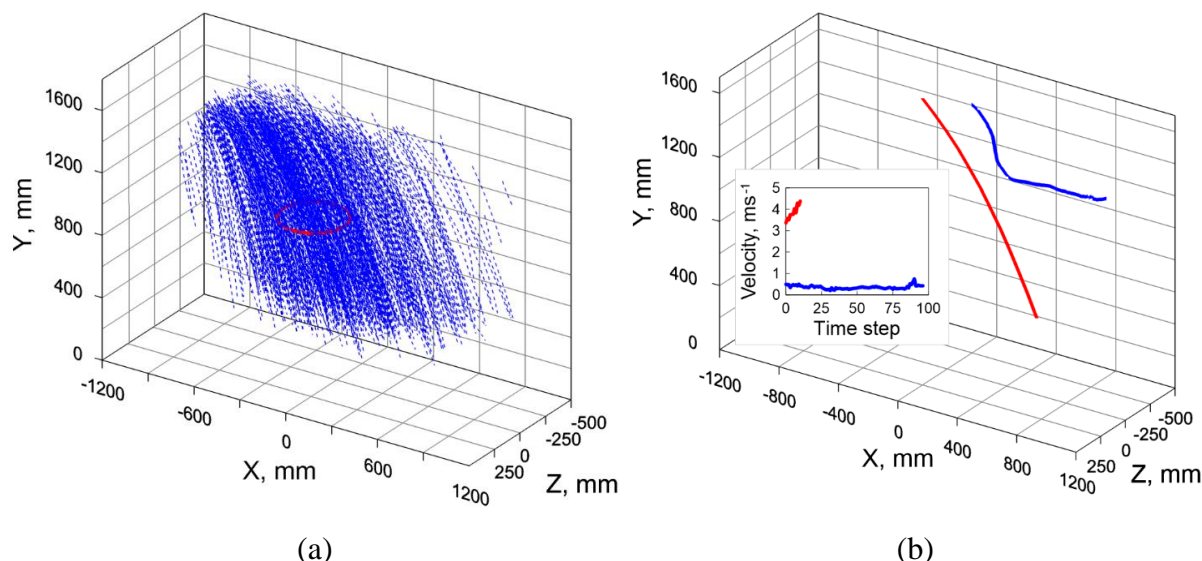
Fig. 21. (a) Cumulated plot of firebrand 3D trajectories (trajectories are plotted with dotted lines to enhance legibility. The red circle defines the perimeter of the reference surface chosen for the particle number flux analysis, see Fig. 22. Center of the reference surface is located at X = -150 mm, Y = 1000 mm, and Z = 0 mm and its radius is equal to 200 mm); (b) Examples of reconstructed trajectories showing the range of firebrand dynamics resolved by the system (inlay shows the corresponding velocity magnitudes, data is shifted horizontally so that the first timesteps are matched). Note that the "slow" firebrand trajectory (blue line) does not show on Fig. (a) since it is filtered out by the mean displacement operator (see Sec. 2.3.3).
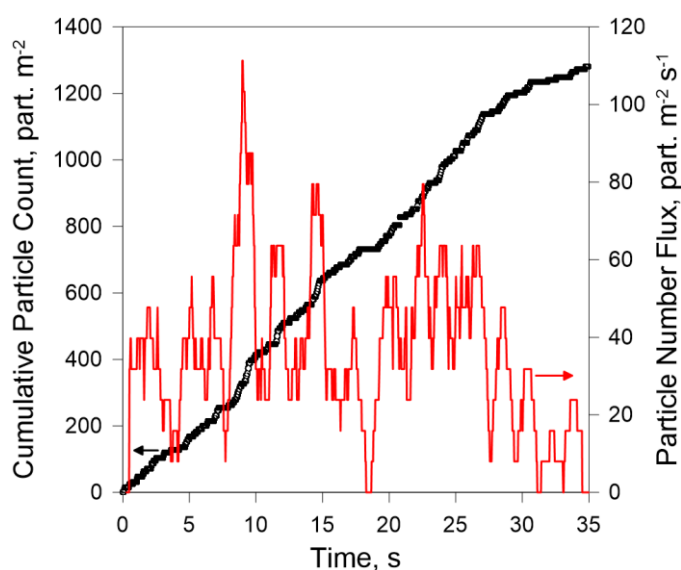
Fig. 22. Cumulative Particle Count and corresponding Particle Number Flux versus time (derivations performed on a 30 timestep window, ≈ 1s). The reference surface outline is shown in Fig. 21a.

A complete characterization of the exposure therefore implies mapping both CPC and PNF distributions as functions of the reference surface orientation. To do so, the orientation of the reference surface is gradually changed by fixed angular increments (keeping the center of the surface constant – see additional details below) and the corresponding CPC/PNF datasets, such as shown in Fig. 22, are retrieved. These can be used to generate a 3D histogram (see Fig. 23), hereby referred to as "firebrand rose" (for its conceptual similarity with wind rose graphics), which delivers a synoptic view of the firebrand exposure over the entire test duration (in the present case, representative of the firebrand shower core). The properties of the arrows that constitute the 3D firebrand rose are as follows:

(1) orientation: indicate the reference surface orientation set by both polar (θ) and azimuthal (φ) angles of the spherical coordinate system depicted in the insert of Fig. 23; the reference surface lays in a plane parallel to the arrow top surface. The center of the reference surface coincides with the origin of the spherical coordinate system. The angular increment is 15° in all directions;

(2) length: total CPC over the entire test duration. The white circles in the sphere median plane indicate CPC iso-lines and the corresponding values are provided. The radius of the outer spherical mesh matches the highest total CPC in any direction (i.e. 1329 particles m^{-2}).

(3) colored bins: each arrow is divided in several bins whose colors correspond to the PNF ranges specified by the color bar located to the right of the 3D histogram. The length of each bin is proportional to the cumulative time for which a PNF in the range indicated by the color was observed at the reference surface. The length of an arrow represents 100 % of the test duration.

The firebrand rose displays an apparent symmetry about the *xy* plane of the spherical coordinate system which is consistent with the experimental configuration and the fact that the flow dynamics stay unchanged during the entire duration of the test. The most severe exposure is obtained for orientations spanning ($\theta = 15°$, $\varphi = 225°$-$285°$) where total CPCs up to 1329 particles m^{-2} are recorded. These orientations correspond to "optimal" situations where the bulk of the firebrand trajectories is mostly normal to the reference surfaces considered. For those cases, PNFs are higher than 40 particles m^{-2} s^{-1} for cumulated time periods exceeding a third of the entire test duration. Taking the case ($\theta = 90°$, $\varphi = 270°$), which corresponds to a vertical surface parallel to the firebrand generator exit plane, the total CPC is found to drop down to $\approx$ 573 particles m^{-2}, with virtually no time period with PNFs higher than 40 particles m^{-2} s^{-1}. This comparison highlights the importance of scrutinizing the firebrand exposure problem in 3D and hence the usefulness of the firebrand rose representation. This is particularly relevant in practical situations whenever exposure severity assessment might be desired, for instance investigating building components with various orientations in space (e.g., gable vents, decking elements, roofing elements, etc.). In addition, the firebrand rose representation, because of its integrated format, is expected to facilitate comparisons between firebrand shower exposures arising from complex field situations that would be otherwise difficult to comprehend solely based on a 3D motion re-construction. These situations might include strong multidirectional motions of firebrands caused by abrupt wind changes, simultaneous lofting/deposition of small/large firebrands involving multiple generation spots, etc.

31
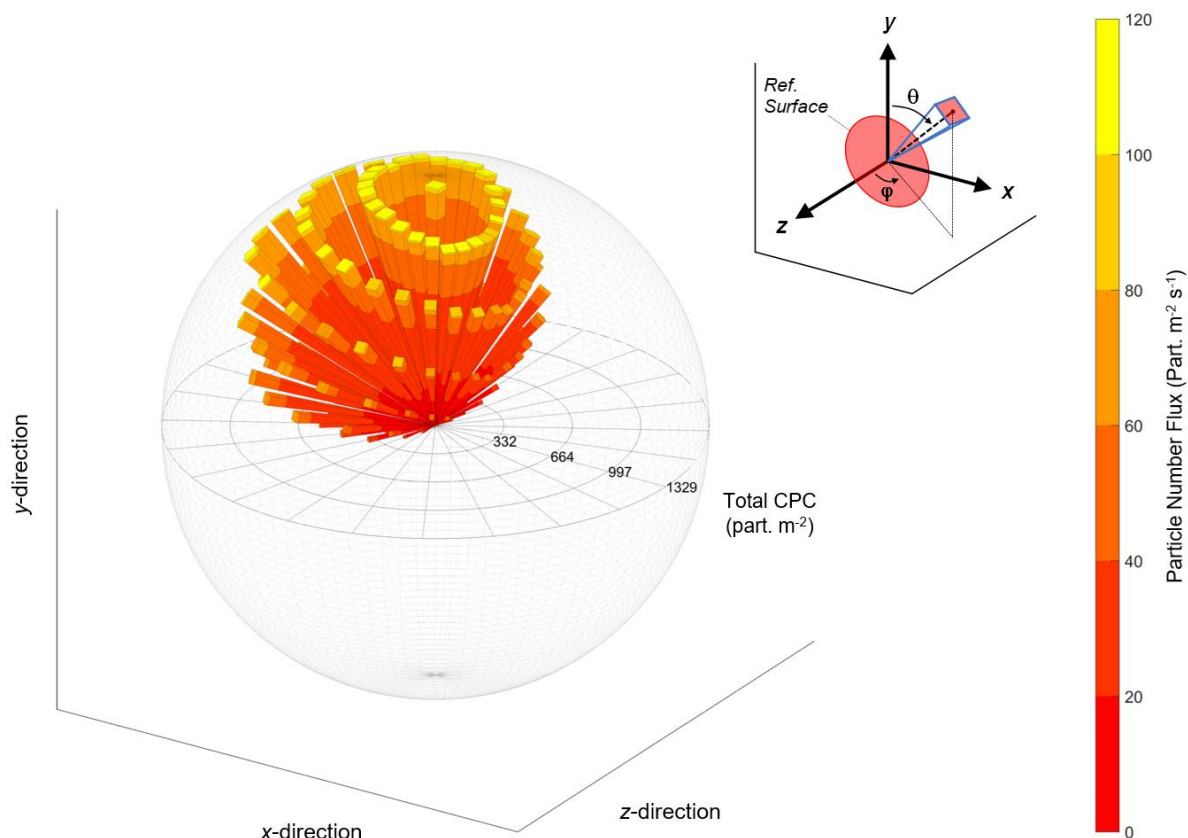
Fig. 23. 3D "firebrand rose" graphic applied to the case presented in Sec. 4. The 3D arrow properties indicate the following: (1) orientation: orientation of the reference surface considered (all references surfaces centered at X = -150 mm, Y = 1000 mm, and Z = 0 mm with r = 200 mm. Orientations are specified using a spherical coordinate system as depicted in the upper right insert, using 15° angular increments); (2) length: particle number collected per m^2 (total CPC) given a reference surface orientation (the radius of the outer spherical mesh matches the highest number of particle collected, i.e. 1329 particles m^{-2}); (3) color-coded bin width: percentage of the total test duration for which the reference surface considered experiences a particle number flux magnitude included in the range specified by the color filler (see color bar legend to the right).

4.2.2. Artificial versus real wildland firebrand exposure: a comparison

The time-resolved characterization of firebrand flows rendered possible by the present system also sets an opportunity for assessing how realistic artificially-generated firebrand fluxes are, with respect to prescribed or actual fire events. This is particularly relevant since there has been a growing interest in using firebrand generators in recent fire studies (e.g., [59, 60]). However, it is generally unclear if the exposure levels generated match those encountered in wildland/WUI fires and when looked at in more detail, the question is solely addressed considering metrics that are uncorrelated with the firebrand flow dynamics and flux intensities (e.g., particle projected area vs mass, see Ref. [58]). While one must acknowledge that field data devoted to firebrand shower characterization is rather scarce at the moment, it is possible, under certain conditions, to perform meaningful firebrand flux comparisons between

32

artificially-generated and actual firebrand flows. An example is provided in the following by considering the present case and the recent investigation of Thomas et al. [29], for which firebrand generation was studied during a prescribed fire (the reader is referred to Ref. [29] for details regarding the experimental configuration). In their work, the authors were able to provide actual durations for the period of peak firebrand collection, and these were found to vary between 67 s and 122 s depending on the collection site. These durations can be used, instead of the more conventional "duration of collection" (defined in Ref. [29] as the time elapsed between the arrivals of the first and last firebrands at monitored spots) to yield conservative[5] firebrand flux estimates that are not biased by periods of low firebrand activity. Doing so suggests that the highest firebrand flux experienced in Ref. [29] was at most 7 particles m^{-2} s^{-1}. This exposure level can be compared to the one achieved in the present case provided that the corresponding PNF (as defined previously) is extracted for matching conditions: (1) the reference surface orientation matches a ground collection configuration, i.e. ($\theta = 0°$, $\varphi = 0°$); (2) the height at which the reference surface is located matches a collection height of 120 mm (height of the collection cans in Ref. [29]). In the present case, data is not directly available at this specific height, but the corresponding time-averaged PNF can be extrapolated using PNF datasets obtained at various heights in the core flow to account for the particle flow divergence. A PNF slightly higher than 24 particles m^{-2} s^{-1} is found, which is more than 3 times the maximum exposure estimated for Ref. [29]. This result highlights the need for proper characterization of artificially generated firebrand flows whenever specific exposure conditions are to be replicated.

4.2.3. Firebrand 3D sizing

Figure 24 shows firebrand size distribution comparisons based on the emberometer measurements (*Airborne* firebrands, white histograms) and the measurements taken on the firebrand population collected in the water pans (*Collected* firebrands, black histograms). In the latter case, given the 2D nature of the size analysis (see Fig. 19b), only two dimensions, respectively labelled *Collected y* and *Collected z*, are used for the comparisons. Results pertaining to the combusting cuboids case detailed in the present section are displayed in the column (a). Results obtained for combusting sticks (pristine particle diam.: 6.6 mm ± 0.3 mm, length: 50.6 mm ± 0.1 mm) detailed in a preliminary study [53] are displayed in the column (b). The side by side comparison of the size distributions obtained for fuel batches with drastically different particle geometries allows to build confidence in the approach by identifying common areas of success and failure. It can be seen in Fig. 24 that the firebrand size distributions agree very well for two of the firebrand dimensions considered: the longest dimension, measured along the particle y-axis (1st row of Fig. 24) as well as one of the smaller dimensions (airborne *x* – see 3rd row of Fig. 24). This agreement is remarkable given the very narrow size class width selected (1 mm). Size distributions along the particle z-axis (2nd row of Fig. 24) suggest however that some of the emberometer measurements overestimate the actual firebrand size in this specific direction. This discrepancy, observed for both combusting cuboids and sticks, is the result of the nonsystematic artifact affecting the particle 3D reconstruction, as described earlier in Sect. 3.2. Note that in the present case, particle shrinkage due to combustion is not likely to be a factor that could explain the mismatch of the z-axis distributions, since the average flight time of a particle from the center of the control volume to the ground is on the

---

[5] The total number of firebrands collected for the entire duration of collection is used since no count of firebrand is provided for the firebrand shower peak events only.

order of 0.3 s. Particle breakage is also unlikely to play a significant role since size distribution in the other directions would have been equally affected.
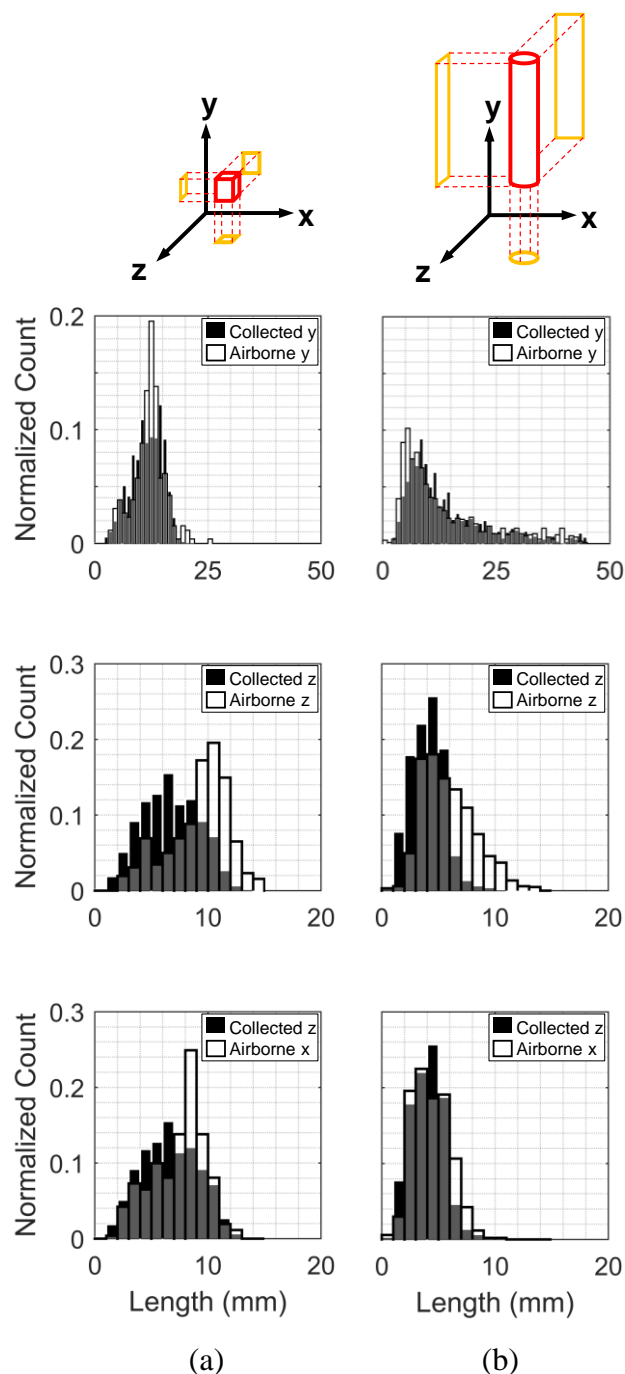
Fig. 24. Firebrand size distributions measured by the 3D-PTV/PSR system (airborne measurements, in white) versus 2D ground collection analysis (water-quenched embers, in black), histogram overlap is shown in gray; case (a): combusting cuboids, case detailed in Sec 4; case (b): combusting sticks, results taken from Ref. [53] and re-plotted for ease of comparison. Schematics in the first line provides an example of particle orientations used for sizing operations.

5. Final Remarks

While the discussion provided in Sec. 4.2 essentially tackles the firebrand shower exposure in term of number fluxes, the ability of the system to resolve individual particle volumes permits mass flux estimations provided that a particle average density is known. This knowledge could be inferred from previous firebrand studies, e.g. [61, 62]. Alternatively, investigating possible scaling relations between the mass of a particle and its morphological attributes might be rewarding: Tohidi et al. [63] pointed out that the mass and surface area of cylindrical firebrands produced from the burning of coniferous trees were correlated and this result was used in Ref. [26] to yield mass flux estimates. Since the approach developed in this work allows for the use of complex 3D particle shape descriptors, developing an analysis similar to that presented in Ref. [63] and that would include some of these descriptors, deserves further scrutiny. In a real WUI fire context, the unknown nature of the firebrands (vegetative and/or structural matter) and their unknown thermal history (char vs pristine fuel content) renders accurate mass flux estimates extremely challenging.

As discussed in the course of this work, the performance of the Visual Hull technique is related to a broad range of factors (particle- and system-specific). Among these, the camera 3D positions and their orientation angles play an essential role. While the present camera layout has been selected to ensure system compactness (enhanced portability for deployment) and minimize measurement intrusiveness, it does not necessarily lead to the smallest hull reconstruction errors. Bringing one of the cameras away from the current acquisition plane can substantially improve the reconstruction process. This is illustrated in Fig. 25 where a fictitious spherical particle (25.4 mm diameter) is moved across the control volume and its visual hull systematically reconstructed. The operation is performed for two different positions of Camera #4, including its original position (0.934 m, 0.312 m, 1.24 m) and a new "out-of-plane" position (0.934 m, 1.033 m, 0 m) located to the right end side of the system control volume. The normalized particle volume (ratio of the reconstructed to the actual volume) is plotted as a function of the effective distance $\bar{D}$, defined as the average of the distances from the camera perspective centers to the center of the particle. It can be seen in Fig. 25 that most of the datapoints for the new Camera #4 location are contained below the 15 % volume overestimation level. This constitutes a marked improvement as compared to the results obtained for the original location (see inlays in Fig. 25 showing examples of reconstructed hulls). Future work will focus on optimizing camera placements to reach optimal hull reconstruction accuracy while maintaining system portability/non-intrusiveness. Some of the criteria proposed by Forbes in Ref. [44] will be further investigated.

For a chosen camera configuration (finite number of cameras, known camera locations and known optical arrangement), the accuracy of the Visual Hull approach only depends on the particle specifics, i.e. the shape and size of the particle, its position within the monitored volume and its orientation. Except for the 3D position, these characteristics are unknown a priori for a random particle in motion, hence the extent to which the visual hulls are affected by reconstruction artifacts, as described in Sec. 3.2, is also unknown. Better understanding reconstruction errors introduced at each time step is essential to correct/remove any bias affecting the particle outline plots and, in fine, increase particle sizing robustness. Based on the discussion above, it is clear that the particle sizing methodology developed here could greatly benefit from the following iterative approach involving particle shape classification: (1) the methodology detailed in Sec. 2.4 is applied. The particle visual hull is reconstructed at

35

each time step and the particle cumulative outline plots, as shown in Fig. 11b, are generated; (2) Similar to the work described by Rajagopalan et al. [47], relevant 2D/3D particle shape descriptors are applied to the outputs of Step 1 and the results are fed to a particle shape classifier adequately trained using supervised learning; the particle shape is matched to that of a generic class (e.g., sphere, quasi-equant, platelet, stick, etc.). A look up table for the measurement errors would be pre-computed by performing series of visual hull reconstructions of a representative fictitious particle, with the particle 3D position, orientation and a size magnification factor as input variables. The metric considered could be the particle volume (hence the data contained in the look-up table would be similar to that shown in Fig. 25 for a sphere) or the particle characteristic sizes, as addressed in the previous sections. (3) The shape of the studied particle being now identified, the proper look-up table can be selected, and the hull reconstruction quality assessed at all timesteps. Data processing strategies to minimize the influence of the reconstruction artifacts can then be applied. These include, for instance, discarding particle hulls that are likely to be prone to substantial reconstruction errors or developing sets of correction factors for the metric considered; (4) Final particle measurements are extracted from the high-fidelity output of step 3. The validity and ease of implementation of such an approach needs further confirmation. Some of the Machine Learning tasks involved in step 2 (e.g., training of the shape classifying algorithm using real firebrand populations) would require dedicated field data collection.
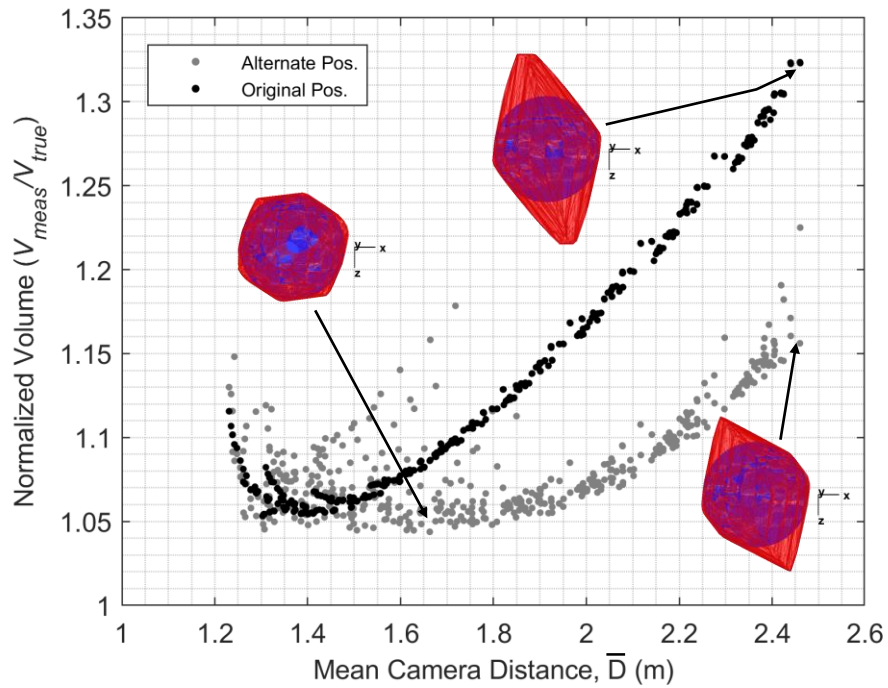
Fig. 25. Normalized volume (ratio of the reconstructed V_{meas} to the known V_{true} volumes) versus $\overline{D}$ (average of the distances from the camera perspective centers to the particle center) for a 25.4 mm fictitious sphere walked through the system control volume. Black dots: Camera #4 coordinates are (0.934 m, 0.312 m, 1.24 m) – original position; gray dots: Camera #4 coordinates are (0.934 m, 1.033 m, 0 m) – new position. Figure inlays show actual (blue) and reconstructed (red) volumes over imposed.

6. Conclusion

A new three-dimensional (3D) measurement diagnostic tool, devoted to the characterization of airborne firebrands in the context of wildland and Wildland-Urban Interface (WUI) fires, has been developed. This tool, referred to as "emberometer", merges the following two imaging techniques: 3D Particle Tracking Velocimetry (3D-PTV), allowing for the time-resolved mapping of firebrand trajectories, and 3D Particle Shape Reconstruction (3D-PSR), used to build 3D models of individual firebrands based on the Visual Hull concept. This emberometer, designed as a self-contained/field-deployable system, offers the possibility to study time-resolved firebrand fluxes and firebrand size distributions to the full extent of their three-dimensional nature, for the first time removing the limitations of the ground collection approach.

The methodologies used in the present work were first validated in laboratory scale experiments, two of which have been reported herein: (1) a particle tracking validation, involving a setup with a lit punk stick with known trajectory and speed, and (2) a particle sizing validation, performed on a series of randomly released spheres (gravity-driven motion) with known diameters. In both cases, measurements were found to closely agree with the benchmark values, with the exception of the sphere size distribution along the particle y-axis for the sizing validation (measurement overestimation). The observed discrepancy was traced back to the presence of extra volumes along the y axes of the particle hulls, a reconstruction artifact due to the current camera layout.

The emberometer was applied to a firebrand shower artificially generated at NIST National Fire Research Laboratory. The motions of nearly 700 firebrands were successfully reconstructed in 3D over a narrow time frame (35 s). The system was able to resolve a wide range of firebrand dynamics, with particle velocities ranging from tens of cm s^{-1} to several m s^{-1}. A novel 3D graphic representation that provides a synthetic view of the firebrand exposure magnitude was introduced. This representation incorporates both the Cumulative Particle Count (CPC, particles m^{-2}) and Particle Number Flux (PNF, particles m^{-2} s^{-1}) as orientation-dependent metrics, and hence is expected to facilitate exposure comparisons across different experiments. Its usefulness was illustrated by comparing the exposure level achieved in the present case to that of an experimental outdoor fire. Firebrand size distributions were also investigated and compared to a case previously discussed. Results showed that excellent agreement between the airborne (emberometer) and ground collection approaches is generally achieved for two of the three firebrand characteristic dimensions. However, size distributions for the third dimension were found to be skewed towards larger sizes, which was attributed to the Visual Hull reconstruction artifact previously mentioned. Strategies to minimize this artifact, by modifying the current camera layout and performing systematic firebrand shape classification, were detailed.

Acknowledgements

References

[1]   Jolly WM, Cochrane MA, Freeborn PH, Holden ZA, Brown TJ, Williamson GJ, Bowman DMJS (2015) Climate-induced variations in global wildfire danger from 1979 to 2013. *Nat Commun* 6:7537. https://doi.org/10.1038/ncomms8537

[2]   Calfire (2019) *Top 20 most destructive California wildfires*. Available at https://www.fire.ca.gov/media/5511/top20_destruction.pdf.

[3]   Yue X, Mickley LJ, Logan JA (2014) Projection of wildfire activity in southern California in the mid-twenty-first century. *Clim Dynam* 43(7):1973-1991. https://doi.org/10.1007/s00382-013-2022-3

[4]   Kitzberger T, Falk DA, Westerling AL, Swetnam TW (2017) Direct and indirect climate controls predict heterogeneous early-mid 21st century wildfire burned area across western and boreal North America. *PLOS ONE* 12(12):e0188486. https://doi.org/10.1371/journal.pone.0188486

[5]   Thomas D, Butry D, Gilbert S, Webb D, Fung J (2017) The costs and losses of wildfires - A literature review. (National Institute of Standards and Technology, Gaithersburg, MD), NIST Special Publication 1215. https://doi.org/10.6028/NIST.SP.1215

[6]   Bermudez E, Panzar J, Oreskes B, Smith D, Shyong F (Oct. 15th 2017) A Santa Rosa woman died in the fires, her neighbors survived. Here are their stories. Los Angeles Times. Available at https://www.latimes.com/projects/la-me-santa-rosa-hemlock/.

[7]   Maranghides A , Mell W (2009) A case study of a community affected by the Witch and Guejito fires. (National Institute of Standards and Technology, Gaithersburg, MD), NIST Technical Note 1635. https://doi.org/10.6028/NIST.TN.1635

[8]   Maranghides A , Mell WE (2013) Framework for adressing the national wildland urban interface fire problem - Determining fire and ember exposure zones using a WUI hazard scale. (National Institute of Standards and Technology, Gaithersburg, MD), NIST Technical Note 1748. https://doi.org/10.6028/NIST.TN.1748

[9]   Thomas JC, Mueller EV, Hadden RM (2018) Estimating net heat flux from surrogate firebrand accumulations using an inverse heat transfer approach. *Advances in Forest Fire Research 2018*, ed Viegas DX (Imprensa da Universidade de Coimbra, Coimbra), Chapter 4 - Fire at the Wildland Urban Interface pp 769-779. https://doi.org/10.14195/978-989-26-16-506_84

[10]   Hakes RSP, Salehizadeh H, Weston-Dawkes MJ, Gollner MJ (2018) Heating and ignition from firebrand piles. *Advances in Forest Fire Research 2018*, ed Viegas DX (Imprensa da Universidade de Coimbra, Coimbra), Chapter 4 - Fire at the Wildland Urban Interface pp 794-799. https://doi.org/10.14195/978-989-26-16-506_87

[11] Hakes RSP, Salehizadeh H, Weston-Dawkes MJ, Gollner MJ (2019) Thermal characterization of firebrand piles. *Fire Safety J* 104:34-42. https://doi.org/10.1016/j.firesaf.2018.10.002

[12] Urban JL, Vicariotto M, Dunn-Rankin D, Fernandez-Pello AC (2019) Temperature measurement of glowing embers with color pyrometry. *Fire Technol* 55(3):1013-1026. https://doi.org/10.1007/s10694-018-0810-3

[13] Kim DK , Sunderland PB (2019) Fire ember pyrometry using a color camera. *Fire Safety J* 106:88-93. https://doi.org/10.1016/j.firesaf.2019.04.006

[14] Suzuki S, Manzello SL, Hayashi Y (2013) The size and mass distribution of firebrands collected from ignited building components exposed to wind. *Proc Combust Inst* 34(2):2479-2485. http://doi.org/10.1016/j.proci.2012.06.061

[15] Suzuki S , Manzello SL (2016) Firebrand production from building components fitted with siding treatments. *Fire Safety J* 80:64-70. http://doi.org/10.1016/j.firesaf.2016.01.004

[16] Suzuki S , Manzello SL (2019) Investigating effect of wind speeds on structural firebrand generation in laboratory scale experiments. *Int J Heat Mass Transfer* 130:135-140. https://doi.org/10.1016/j.ijheatmasstransfer.2018.10.045

[17] Waterman TE (1969) Experimental study of firebrand generation. (IIT Research Institute, Chicago, IL), Final Technical Report on Project J6130

[18] Manzello SL, Suzuki S, Naruse T (2019) Quantifying wind-driven firebrand production from roofing assembly combustion. *Fire Mater* 43(1):3-7. https://doi.org/10.1002/fam.2661

[19] Yoshioka H, Hayashi Y, Masuda H, Noguchi T (2004) Real-scale fire wind tunnel experiment on generation of firebrands from a house on fire. *Fire Science and Technology* 23(2):142-150. https://doi.org/10.3210/fst.23.142

[20] Suzuki S, Brown A, Manzello SL, Suzuki J, Hayashi Y (2014) Firebrands generated from a full-scale structure burning under well-controlled laboratory conditions. *Fire Safety J* 63:43-51. http://doi.org/10.1016/j.firesaf.2013.11.008

[21] Vodvarka FJ (1969) Firebrand field studies. (IIT Research Institute, Chicago, IL), Final Technical Report on Project J6148

[22] Vodvarka FJ (1970) Urban burns - Full scale field studies. (IIT Research Institute, Chicago, IL), Final Technical Report on Project J6171

[23] Suzuki S, Manzello SL, Lage M, Laing G (2012) Firebrand generation data obtained from a full-scale structure burn. *Int J Wildland Fire* 21(8):961-968. http://doi.org/10.1071/WF11133

[24]   Manzello SL, Maranghides A, Mell WE (2007) Firebrand generation from burning vegetation. *Int J Wildland Fire* 16(4):458-462. http://dx.doi.org/10.1071/WF06079

[25]   Manzello SL, Maranghides A, Shields JR, Mell WE, Hayashi Y, Nii D (2009) Mass and size distribution of firebrands generated from burning Korean pine (Pinus koraiensis) trees. *Fire Mater* 33(1):21-31. https://doi.org/10.1002/fam.977

[26]   Tohidi A, Gollner MJ, Alfano C, Quarles Q (2017) Computer vision techniques for firebrand detection and characterization. *16th International Conference on Automatic Fire Detection and the Suppression, Detection and Signaling Research and Applications (SUPDET 2017)*, (Hyattsville, MD)

[27]   El Houssami M, Mueller E, Filkov A, Thomas JC, Skowronski N, Gallagher MR, Clark K, Kremens R, Simeoni A (2016) Experimental procedures characterising firebrand generation in wildland fires. *Fire Technol* 52(3):731-751. https://doi.org/10.1007/s10694-015-0492-z

[28]   Filkov A, Prohanov S, Mueller E, Kasymov D, Martynov P, Houssami ME, Thomas J, Skowronski N, Butler B, Gallagher M, Clark K, Mell W, Kremens R, Hadden RM, Simeoni A (2017) Investigation of firebrand production during prescribed fires conducted in a pine forest. *Proc Combust Inst* 36(2):3263-3270. https://doi.org/10.1016/j.proci.2016.06.125

[29]   Thomas JC, Mueller EV, Santamaria S, Gallagher M, El Houssami M, Filkov A, Clark K, Skowronski N, Hadden RM, Mell W, Simeoni A (2017) Investigation of firebrand generation from an experimental fire: Development of a reliable data collection methodology. *Fire Safety J* 91:864-871. https://doi.org/10.1016/j.firesaf.2017.04.002

[30]   Filkov A , Prohanov S (2018) Particle tracking and detection software for firebrands characterization in wildland fires. *Fire Technol* 55(3):817-836. https://doi.org/10.1007/s10694-018-0805-0

[31]   Rissel S , Ridenour K (2013) Ember production during the Bastrop complex fire. *Fire Management Today* 72(4):7-13

[32]   Manzello SL , Foote EID (2014) Characterizing firebrand exposure from Wildland–Urban Interface (WUI) fires: results from the 2007 Angora fire. *Fire Technol* 50(1):105-124. https://doi.org/10.1007/s10694-012-0295-4

[33]   Guala M, Liberzon A, Hoyer K, Tsinober A, Kinzelbach W (2008) Experimental study on clustering of large particles in homogeneous turbulent flow. *J of Turbul* 9(34):1-20. https://doi.org/10.1080/14685240802441118

[34]   Maas HG (1991) Digital photogrammetry for determination of tracer particle coordinates in turbulent flow reasearch. *Photogramm Eng Rem S* 57(12):1593-1597

[35] Kim JT, Zhang Z, Liberzon A, Zhang Y, Chamorro LP (2016) On the Lagrangian features of circular and semicircular jets via 3D Particle Tracking Velocimetry. *Exp Therm Fluid Sci* 77:306-316. http://doi.org/10.1016/j.expthermflusci.2016.05.003

[36] Murai Y, Oishi Y, Tasaka Y, Takeda Y (2008) Particle tracking velocimetry applied for fireworks. *J Visual-Japan* 11(1):63-70. https://doi.org/10.1007/bf03181915

[37] Biwole PH, Yan W, Zhang Y, Roux J-J (2009) A complete 3D particle tracking algorithm and its applications to the indoor airflow study. *Meas Sci Technol* 20(11):115403. https://doi.org/10.1088/0957-0233/20/11/115403

[38] Malik NA, Dracos T, Papantoniou DA (1993) Particle tracking velocimetry in three-dimensional flows. *Exp Fluids* 15(4):279-294. https://doi.org/10.1007/bf00223406

[39] Li D, Zhang Y, Sun Y, Yan W (2008) A multi-frame particle tracking algorithm robust against input noise. *Meas Sci Technol* 19(10):105401. https://doi.org/10.1088/0957-0233/19/10/105401

[40] Lobutova E, Resagk C, Putze T (2010) Investigation of large-scale circulations in room air flows using three-dimensional particle tracking velocimetry. *Build Environ* 45(7):1653-1662. http://dx.doi.org/10.1016/j.buildenv.2010.01.016

[41] Rosi GA, Sherry M, Kinzel M, Rival DE (2014) Characterizing the lower log region of the atmospheric surface layer via large-scale particle tracking velocimetry. *Exp Fluids* 55(5):1-10. https://doi.org/10.1007/s00348-014-1736-2

[42] Bastide Bl, Rosi GA, Rival DE (2014) The development of a large-scale particle tracking velocimery system for wake analysis of wind-loaded structures. *J Phys: Conf Ser* 524(1):012172. https://doi.org/10.1088/1742-6596/524/1/012172

[43] Laurentini A (1994) Visual hull concept for silhouette-based image understanding. *IEEE Transactions on Pattern Analysis and Machine Intelligence* 16(2):150-162. https://doi.org/10.1109/34.273735

[44] Forbes K (2007) Calibration, recognition, and shape from silhouettes of stones. Ph.D. thesis. (University of Cape Town, Cape Town). Available at https://www.dip.ee.uct.ac.za/publications/theses/PhDKeith.pdf.

[45] Turchiuli C , Castillo-Castaneda E (2009) Agglomerates structure characterization using 3D-image reconstruction. *Part Part Syst Char* 26(1-2):25-33. https://doi.org/10.1002/ppsc.200700028

[46] Adhikari D , Longmire EK (2012) Visual hull method for tomographic PIV measurement of flow around moving objects. *Exp Fluids* 53(4):943-964. https://doi.org/10.1007/s00348-012-1338-9

[47] Rajagopalan AK, Schneeberger J, Salvatori F, Bötschi S, Ochsenbein DR, Oswald MR, Pollefeys M, Mazzotti M (2017) A comprehensive shape analysis pipeline for

stereoscopic measurements of particulate populations in suspension. *Powder Technol* 321:479-493. https://doi.org/10.1016/j.powtec.2017.08.044

[48]   Kleinkort C, Huang G-J, Bringi VN, Notaroš BM (2017) Visual Hull method for realistic 3D particle shape reconstruction based on high-resolution photographs of snowflakes in free fall from multiple views. *J Atmos Ocean Tech* 34(3):679-702. https://doi.org/10.1175/jtech-d-16-0099.1

[49]   Garrett TJ, Fallgatter C, Shkurko K, Howlett D (2012) Fall speed measurement and high-resolution multi-angle photography of hydrometeors in free fall. *Atmos Meas Tech* 5(11):2625-2633. https://doi.org/10.5194/amt-5-2625-2012

[50]   Luhmann T, Robson S, Kyle S, Boehm J (2014) *Close range photogrammetry and 3D imaging* (Walter De Gruyter GmbH, Berlin/Boston), Second Ed.

[51]   Maas HG, Gruen A, Papantoniou D (1993) Particle tracking velocimetry in three-dimensional flows. *Exp Fluids* 15(2):133-146. https://doi.org/10.1007/bf00190953

[52]   Willneff J (2003) A spatio-temporal matching algorithm for 3D particle tracking velocimetry. Ph.D. thesis. (Swiss Federal Institute of Technology Zurich, Zurich). Available at https://ethz.ch/content/dam/ethz/special-interest/baug/igp/igp-dam/documents/PhD_Theses/82.pdf.

[53]   Bouvet N, Link ED, Fink SA, Kuligowski ED (2018) On the use of time-resolved three-dimensional diagnostics to characterize firebrand showers in the WUI. *Advances in Forest Fire Research 2018*, ed Viegas DX (Imprensa da Universidade de Coimbra, Coimbra), Chapter 4 – Fire at the Wildland Urban Interface pp 826-836. https://doi.org/10.14195/978-989-26-16-506_91

[54]   *Open PTV Software Consortium, www.openptv.net*. Available at https://doi.org/10.5281/zenodo.2646623.

[55]   Press WH, Flannery BP, Teukolsky SA, Vetterling WT (1992) *Numerical recipes in Fortran 77: the art of scientific computing* (Cambridge University Press, Cambridge), Second Ed.

[56]   Otsu N (1979) A threshold selection method from gray-level histograms. *IEEE Transactions on Systems, Man, and Cybernetics* 9(1):62-66. https://doi.org/10.1109/TSMC.1979.4310076

[57]   Luhmann T (2014) Eccentricity in images of circular and spherical targets and its impact on spatial intersection. *Photogramm Rec* 29(148):417-433. https://doi.org/10.1111/phor.12084

[58]   Manzello SL, Shields JR, Cleary TG, Maranghides A, Mell WE, Yang JC, Hayashi Y, Nii D, Kurita T (2008) On the development and characterization of a firebrand generator. *Fire Safety J* 43(4):258-268. http://doi.org/10.1016/j.firesaf.2007.10.001

[59]   Sharifian A , Hashempour J (2016) A novel ember shower simulator for assessing performance of low porosity screens at high wind speeds against firebrand attacks. *J Fire Sci* 34(4):335-355. https://doi.org/10.1177/0734904116655175

[60]   Quarles SL , Standohar-Alfano CD (2018) Wildfire Research - Ignition potential of decks subjected to an ember exposure. (Insurance Institute for Business & Home Safety), Technical report. https://ibhs.org/wp-content/uploads/Ignition-Potential-of-Decks-Subjected-to-an-Ember-Exposure.pdf

[61]   Sánchez Tarifa C, Pérez Del Notario P, García Moreno F, Rodriguez Villa A (1967) Transport and combustion of firebrands - Volume II. (Instituto Nacional de Tecnica Aeroespacial «Esteban Terradas», Madrid, Spain), Final Report of Grants FG-SP-114 and FG-SP-146 (Vol. II)

[62]   Muraszew A , Fedele JB (1975) Firebrand investigation. (The Aerospace Corporation, El Segundo, California), Aerospace Report no. ATR-75(7470)-1

[63]   Tohidi A, Kaye N, Bridges W (2015) Statistical description of firebrand size and shape distribution from coniferous trees for use in Metropolis Monte Carlo simulations of firebrand flight distance. *Fire Safety J* 77:21-35. http://doi.org/10.1016/j.firesaf.2015.07.008

Appendix A – Estimation of Variable Uncertainties

Table A1 Uncertainty estimates for the main variables considered in the present work. All estimates provided correspond to expanded uncertainties with a 95% level of confidence or greater.

Variable	Uncertainty	Notes
Particle 3D position (X, Y, Z)	± 1.5 mm in all directions	• Estimated during the spatial calibration procedure. • Assumes uniform pixel intensity across particle silhouettes (i.e., no bias in particle centroid detection).
Particle speed	± 1 %	• Major contribution arises from particle positioning uncertainty (negligible temporal shifts). • Applies to most common firebrand trajectories discussed in Sec. 4.
Cumulative Particle Count (CPC)	- 0 %, + 4 %	• Major contribution arises from broken particle trajectories (negligible temporal shifts). • Occurrence of broken trajectories assumed to be random in space and time. • Value might be affected if experimental conditions significantly deviate from the current ones (e.g., change in tracking efficiency).
Particle Number Flux (PNF)	- 0 %, + 4 %	• Same as above. • Valid given a fixed temporal derivation window.
Particle size	± 2 mm (x- and y-axes) - 5 mm, + 0 mm (z-axis)	• Applies to the measurements given in Fig. 24a (cuboid firebrands). • Uncertainty to depend on particle size/shape and motion, therefore, requires case by case consideration. • z-axis measurements are affected by the Visual Hull reconstruction artifact.